Synaptic plasticity in human thalamocortical assembloids

Authors

Mary H. Patton[1,†], Kristen T. Thomas[1,†], Ildar T. Bayazitov[1], Kyle D. Newman[1], Nathaniel B. Kurtz[2], Camenzind G. Robinson[2], Cody A. Ramirez[1], Alexandra J. Trevisan[1], Jay B. Bikoff[1], Samuel T. Peters[3], Shondra M. Pruett-Miller[3,4], Yanbo Jiang[1], Andrew B. Schild[1], Anjana Nityanandam[1], Stanislav S. Zakharenko[1,*]

Affiliations

[1]Department of Developmental Neurobiology, St. Jude Children's Research Hospital; Memphis, TN 38105, USA

[2]Cell and Tissue Imaging Center, St. Jude Children's Research Hospital; Memphis, TN 38105, USA

[3]Center for Advanced Genome Engineering, St. Jude Children's Research Hospital; Memphis, TN 38105, USA

[4]Department of Cell & Molecular Biology, St. Jude Children's Research Hospital; Memphis, TN 38105, USA

[*]Corresponding author: Stanislav S. Zakharenko, stanislav.zakharenko@stjude.org

[†]These authors contributed equally to this work.

Highlights

- Human thalamic organoids consist of mostly glutamatergic projection neurons.
- Thalamocortical assembloids form reciprocal glutamatergic synapses.
- Synapses are functional and undergo short-term plasticity resembling animal models.
- Long-term potentiation and depression reveal mechanisms distinct from rodents.

eTOC

Human organoids are often used to model diseases with synaptic pathology; however, few studies have examined synaptic function via single-cell or single-synapse recordings. Patton et al. fused human thalamic and cortical organoids into assembloids to examine synaptic transmission and short- and long-term synaptic plasticity in human thalamocortical and corticothalamic circuits.

35 **GRAPHICAL ABSTRACT**

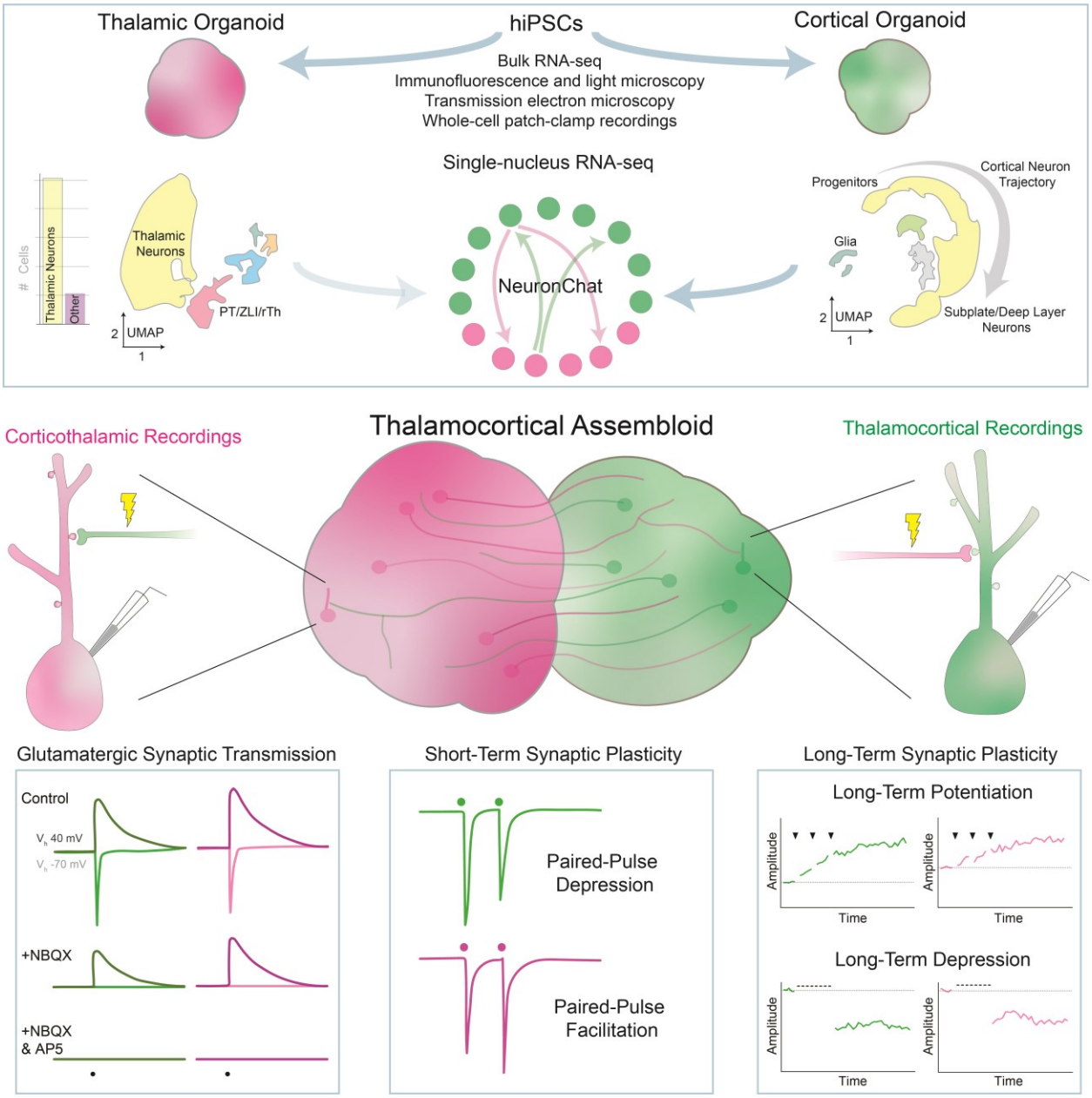

36

SUMMARY

Synaptic plasticities, such as long-term potentiation (LTP) and depression (LTD), tune synaptic efficacy and are essential for learning and memory. Current studies of synaptic plasticity in humans are limited by a lack of adequate human models. Here, we modeled the thalamocortical system by fusing human induced pluripotent stem cell–derived thalamic and cortical organoids. Single-nucleus RNA-sequencing revealed that most cells in mature thalamic organoids were glutamatergic neurons. When fused to form thalamocortical assembloids, thalamic and cortical organoids formed reciprocal long-range axonal projections and reciprocal synapses detectable by light and electron microscopy, respectively. Using whole-cell patch-clamp electrophysiology and two-photon imaging, we characterized glutamatergic synaptic transmission. Thalamocortical and corticothalamic synapses displayed short-term plasticity analogous to that in animal models. LTP and LTD were reliably induced at both synapses; however, their mechanisms differed from those previously described in rodents. Thus, thalamocortical assembloids provide a model system for exploring synaptic plasticity in human circuits.

INTRODUCTION

Synaptic transmission through the release of neurotransmitter and the subsequent activation of postsynaptic receptors is the fundamental mode of communication between neurons. Synaptic plasticity enhances or diminishes synaptic transmission in an activity-dependent manner in response to environmental cues. Although the chemical synapse is evolutionarily conserved,[1] the molecular mechanisms underlying synaptic plasticity differ across species.[2–6] Aberrant synaptic plasticity is well documented in animal models of autism, schizophrenia, and other psychiatric disorders.[7–10] Ultimately, these human disorders would benefit from a human model system.

Ex vivo human model systems are currently limited to postmortem samples, which are often in a state of uncertain tissue quality, and biopsy samples, which are almost exclusively from individuals with epilepsy or brain tumors.[11] The recent development of human induced pluripotent stem cell (hiPSC)-derived organoids provides a promising *in vitro* model system that is accessible to experimental manipulation and recapitulates human-specific features of neural development and function.[12–18] Organoids are widely used to model synaptopathies (i.e., neurologic and psychiatric disorders associated with synaptic dysfunction).[19–25] Specific properties of synaptic transmission and synaptic plasticity differ across brain regions and neuronal subtypes;[2,26–28] however, few studies have examined synaptic transmission between defined pre- and postsynaptic cell populations in organoids.[29–31] Moreover, synaptic plasticity within organoids has never been reported using whole-cell patch-clamp electrophysiology, the gold standard approach for studying synaptic physiology that has been validated over decades of research in animal models.

To build a functional neural circuit, human cortical organoids (hCOs) can be fused with human thalamic organoids (hThOs) to produce thalamocortical (TC) assembloids.[32] The thalamus is a primary relay center for incoming sensory information that sends widespread, yet highly organized, projections to various cortical regions based on the sensory modality.[33–36] The cortex, in turn, sends projections back to thalamic nuclei to integrate and update sensory, motor, and

77 cognitive information.[37,38] Collectively, synaptic transmission within the thalamo–cortico–thalamic
78 circuit creates cognitive representations of the outside world based on diverse incoming sensory
79 inputs and provides the foundation for dynamic executive functioning.[39–42] Experience-dependent
80 synaptic plasticity within this system is critical to learning and underlies the expression of
81 sensorimotor behaviors, attention, and perceptual and working memory.[42–47]

82 Here we developed a human assembloid system containing functional glutamatergic TC
83 and corticothalamic (CT) synaptic connections that undergo short- and long-term synaptic
84 plasticity. We then used this system to explore the molecular mechanisms underlying synaptic
85 plasticity in human neurons.

86

87 **RESULTS**

88 **hThOs contain functional glutamatergic thalamic neurons**

89 To build optimal hThOs, we generated a reporter line from an hiPSC line derived from a
90 neurotypical male subject with normal karyotype (See **Figure S1** for reporter line validation).
91 Specifically, the *tdTomato*-coding sequence was inserted into the endogenous *TCF7L2* locus
92 (**Figure 1A**). We then modified a previously reported protocol[32] to increase the efficiency of
93 thalamic neuron generation. After differentiation into hThOs, we performed bulk RNA-sequencing
94 and then VoxHunt deconvolution analysis of the RNA-seq data. High *tdTomato* RNA levels
95 identified hThOs with high representation of diencephalon, the developmental structure that gives
96 rise to the thalamus, and low representation from contaminating structures, e.g., the pallium and
97 midbrain (**Figure 1A**). Notably, in hThOs generated from five independent hiPSC lines, *TCF7L2*
98 positively predicted the expression of the thalamic neural precursor genes *OLIG3* and *OTX2* and
99 the thalamic neuron genes *GBX2* and *LHX9* (**Figure S2**). Visual assessment was sufficient to
100 identify hThOs with high *tdTomato*, as differential expression analysis comparing hThOs with high
101 TCF7L2-tdTomato fluorescence to hCOs revealed significant enrichment of thalamic markers in

102 the hThOs (**Figure S3A** and **S3B**). All subsequent experiments were performed with TCF7L2-
103 tdTomato$^+$ hThOs.

104 At 60 days after the start of differentiation (D60), hThOs contained OTX2$^+$ and SOX2$^+$
105 neural progenitor domains surrounded by TUBB3$^+$ neurons (**Figure 1B**). By D92, most cells
106 expressed markers consistent with glutamatergic neurons of the developing thalamus, specifically
107 LHX2, FOXP2, and GBX2; GABA immunoreactivity was observed in only a small subset of cells
108 (**Figure S3C**). At D70–D90 in culture, synaptic gene expression significantly increased, and
109 precursor and mitotic gene expression decreased in hThOs (**Figure S3D and S3E**).

110 Single-nucleus RNA-sequencing (snRNA-seq) analysis of D90 hThOs revealed that the
111 majority (~85%) of cells were glutamatergic neurons found primarily in Excitatory Neuron 1-4
112 (ExN1-4) clusters (**Figure 1C-1F**). Applying VoxHunt mapping to *BrainSpan* and *Allen Brain Atlas*
113 references, we found that clusters ExN1-4 mapped to the human mediodorsal thalamus (**Figure**
114 **1D**) and embryonic day (E) 15 mouse caudal thalamus (**Figure 1G**), the diencephalon structure
115 that produces the glutamatergic neurons of the mature thalamus. Consistent with thalamic
116 neurons, ExN1-4 neurons primarily expressed *SLC17A6* (or *VGLUT2*); *SLC17A7* (or *VGLUT1*)
117 was sparsely expressed (**Figure 1F**). Neurons in clusters ExN1-4 expressed additional thalamic
118 markers of interest, including *GBX2*, *SHOX2*, *FOXP2*, *CADM1*, and *NTNG1* (**Figure S3F**). In line
119 with reports from the mouse thalamus,[48] a subset of cells also expressed *SOX2*, a marker typically
120 associated with precursors rather than mature neurons (**Figure S3F**). We also identified one
121 cluster that mapped to E15 mouse pretectum (PT) (**Figure 1H**), as well as cells expressing
122 markers of the thalamic organizer zona limitans intrathalamica (ZLI) and rostral thalamus (rTh)
123 (**Figure 1I**). Like the caudal thalamus, these structures arise from the diencephalon during early
124 development. A small subset of *SLC17A6*$^+$ glutamatergic neurons and all *GAD1*$^+$ GABAergic
125 neurons within the hThOs were found in this PT/ZLI/rTh cluster.

126 To verify that most cells in hThOs were functional neurons, we used whole-cell patch-
127 clamp electrophysiology to investigate the membrane properties of individual cells. Action

128 potentials (APs) were evoked in response to depolarizing current injections (**Figure 1J**). The
129 resting membrane potential, membrane capacitance, input resistance, and AP properties
130 measured in hThO cells were consistent with functional neurons (**Figure S4A-S4H**). Transmission
131 electron microscopy (TEM) also revealed numerous asymmetric and symmetric synapses in
132 hThOs (**Figure S4Q** and **S4R**). A subset of presynaptic terminals contained dense core vesicles
133 (**Figure S4S**).

134 Finally, we examined the non-neuronal cell populations in our hThOs. Pseudotime
135 analysis (**Figure 1K**) and cell cycle analysis (**Figure 1L-1N**) revealed a small cluster of precursor
136 cells undergoing mitosis (i.e., Cycling Progenitors cluster). *TNC*$^+$ progenitors not undergoing
137 mitosis were labeled radial glia. Most of the remaining cells were *GFAP*$^+$ astrocytes within the
138 Glia cluster (**Figure 1O**). Pseudotime analysis also revealed differences in glutamatergic neuron
139 maturity, with the ExN4 cluster containing the least mature thalamic neurons, and the ExN2
140 cluster containing the most mature thalamic neurons (**Figure 1K**). We conclude that our hThO
141 protocol generated functional thalamic neurons with high efficiency, and that those neurons
142 formed synaptic connections.

143

144 **TC assembloids form functional glutamatergic TC and CT synapses**

145 To form TC assembloids, we also required optimal hCOs. We generated an isogenic hiPSC
146 reporter line by inserting the *tdTomato*-coding sequence into the endogenous *SLC17A7*
147 (*VGLUT1*) locus (**Figure 2A**) (See **Figure S1** for reporter line validation). Using this reporter line,
148 we generated hCOs via a previously reported protocol.[49] Voxhunt deconvolution analysis of bulk
149 RNA-seq data demonstrated that VGLUT1-tdTomato$^+$ hCOs exhibited high representation of the
150 pallium, the developmental structure that gives rise to the neocortex, and low representation of
151 contaminating structures, e.g., the subpallium and diencephalon (**Figure 2A**). High expression of
152 *tdTomato* RNA also predicted high expression of cortical markers relative to hThOs (**Figure S3A**

153 and **S3B**) and VGLUT1-tdTomato^{-} hCOs (**Figure S5A**). All subsequent experiments were
154 performed with VGLUT1-tdTomato^{+} hCOs.

155 The snRNA-seq analysis of D90 hCOs revealed that most cells fell within a neuronal
156 developmental trajectory, beginning with neural precursors and ending with differentiated neurons
157 that expressed markers of upper-layer (UL) or deep-layer (DL) excitatory cortical neurons (UL
158 ExNs and DL ExNs, respectively) (**Figures 2B** and **S5**). Using VoxHunt mapping to *BrainSpan*
159 and *Allen Brain Atlas* references, we found that clusters within this trajectory mapped to human
160 neocortical structures (**Figure S5B**) and E15 mouse neocortex (**Figure 2C**). During early
161 development, thalamic neurons first form synapses with the cortical subplate before transitioning
162 to cortical Layer IV.[50] We identified a cluster in hCOs (Subplate/DL ExN) that was enriched for
163 markers of the cortical subplate[51] (**Figure 2B**) and contained the most mature neurons based on
164 pseudotime analysis (**Figure 2D**), which was in line with this cluster containing subplate-like
165 neurons.[52] Consistent with previous reports in rodent models,[53] *SLC17A6* was expressed in
166 intermediate progenitors, but expression declined with neuronal maturation (**Figure 2E**). Mature
167 neurons in hCOs exclusively expressed *SLC17A7* (**Figure 2F**). Remaining cells included
168 unidentified glutamatergic neurons (found in the Un.ExN1 and Un.ExN2 clusters), glia, and cells
169 resembling those in choroid plexus (**Figure S5I and S5J**).

170 We investigated the firing properties of hCO cells by using whole-cell patch-clamp
171 electrophysiological recordings. Delivering depolarizing current injections to hCO cells evoked AP
172 firing (**Figures 2F** and **S4L-S4P**). These cells also displayed typical neuronal properties (**Figure**
173 **S4I-S4P**). TEM revealed numerous asymmetric and symmetric synapses in hCOs (**Figure S4Q**
174 and **S4R**). A subset of presynaptic terminals contained dense core vesicles (**Figure S4S**).

175 We then fused hThOs with hCOs to form TC assembloids. The hCOs were transduced
176 with hSyn-GFP lentivirus prior to fusion, so each organoid could be identified within the
177 assembloid (**Figure 2G**). GFP^{+} axons from the hCO were detectable within the hThO within 5

178 days postfusion (dpf). Furthermore, 2-dimensional fusion assays confirmed that hThOs and hCOs
179 sent reciprocal axonal projections (**Figure 2H**).

180 We then sought to identify TC and CT synapses formed between the organoids after
181 fusion. To that end, we transduced either the hThO or hCO with hSyn-V5-Mito-APEX2 lentivirus,
182 which localized the V5-tagged peroxidase APEX2 to the mitochondrial matrix in neurons, enabling
183 the identification of the hThO or hCO origin of the presynaptic terminal.[54] APEX2$^+$ hThOs were
184 fused with APEX2$^-$ hCOs (or vice versa) to form TC assembloids. Light microscopy and
185 immunolabeling identified V5$^+$ puncta that co-localized with neurons expressing hSyn-GFP
186 (**Figure 2I**). Reaction with DAB produced strong contrast in the matrix of APEX2$^+$ mitochondria in
187 TEM images. TEM images revealed APEX2$^+$ mitochondria in presynaptic terminals from the hThO
188 that formed TC synapses within the hCO after fusion (**Figure 2J**). Conversely, we observed
189 APEX2$^+$ mitochondria in presynaptic terminals from the hCOs that formed CT synapses within the
190 hThOs after fusion (**Figure 2K**). This analysis confirmed that assembloids contained both TC and
191 CT synapses.

192 Whole-cell patch-clamp electrophysiology recordings confirmed that these synapses were
193 functional (**Figure 2L-2N**). Electrical synaptic stimulation of the hThO (**Figure 2L**) or hCO (**Figure**
194 **2M**) evoked excitatory postsynaptic currents (EPSCs) in cells recorded in the hCO or hThO,
195 respectively. The likelihood of evoking a synaptic response varied among assembloids (**Figure**
196 **2L** and **2M**); on average, the chance of cells responding to electrical stimulation of the opposite
197 organoid was 61% for the TC synapses and 58% for the CT synapses (**Figure 2M**).

198 To begin characterizing this synaptic response, we calculated the paired-pulse ratio (PPR)
199 of EPSCs, a classic measure of presynaptic short-term plasticity, at TC and CT synapses.[51–57] In
200 response to a pair of stimuli applied to a presynaptic neuron, TC synapses elicited paired-pulse
201 depression, wherein the second postsynaptic response was weaker than the first. In contrast, CT
202 synapses were more prone to paired-pulse facilitation, wherein the second response was stronger

203 than the first (**Figure 2N**). Both results resemble previous observations of these synapses in
204 animal models.[55–61]

205 Next, we investigated the potential cellular origin of the functional connections between
206 hThOs and hCOs. We used NeuronChat[62] to determine the likelihood of neuronal communication
207 between cell clusters in the hThOs and hCOs based on snRNA-seq data. We found that the hThO
208 ExN clusters, which contain glutamatergic thalamic neurons, exhibited the highest probability of
209 TC communication with cells in the Cycling Progenitor and Subplate/DL ExN clusters of the hCOs
210 (**Figure 3A**). Conversely, Subplate/DL ExNs exhibited a higher probability of CT communication
211 with hThO ExN clusters than exhibited by other hCO clusters (**Figure 3B**). NRXN signaling
212 mediates synaptogenesis, whereas glutamate signaling mediates excitatory synaptic
213 transmission. Further analysis revealed that hThO ExNs exhibited a high probability of TC
214 communication with hCO Cycling Progenitors and Subplate DL/ExNs clusters by NRXN signaling
215 (**Figure 3C**). The hCO Subplate/DL ExNs and hThO ExNs also exhibited a higher probability of
216 TC and CT communication using glutamate than other clusters (**Figure 3D**). Our snRNA-seq data
217 confirmed that these clusters expressed the necessary ligands and receptors for NRXN and
218 glutamatergic signal transduction (**Figure S6**). Overall, NeuronChat predicted that TC
219 glutamatergic synaptic transmission most likely occurs between the hThO ExN2 cluster, which
220 contains the most mature thalamic neurons, and the hCO Subplate/DL ExNs. Conversely, CT
221 glutamatergic synaptic transmission most likely occurs between the hCO Subplate/DL ExNs and
222 the hThO ExN1 cluster, the largest cluster containing glutamatergic thalamic neurons.

223 Next, we used whole-cell patch-clamp electrophysiology to further characterize TC and
224 CT synaptic transmission. Evoked TC and CT EPSCs showed typical glutamatergic ionotropic
225 properties comprising a fast α-amino-3-hydroxy-5-methyl-4-isoxazoleproprionic acid receptor
226 (AMPAR)-mediated component blocked by the AMPAR inhibitor NBQX (3 mM) [86.7% ± 3.3%
227 AMPAR current reduction for TC synapses (**Figure 3E** and **3G**); 82.2% ± 3.8% AMPAR current
228 reduction for CT synapses, (**Figure 3H** and **3J**)] and a slow *N*-methyl-D-aspartate receptor

229 (NMDAR)-mediated component blocked by the NMDAR inhibitor AP5 (50 μM) [84.0% ± 4.6%
230 NMDAR current reduction for TC synapses (**Figure 3F** and **3G**); 78.4% ± 2.9% NMDA current
231 reduction for CT synapses (**Figure 3I** and **3J**)].

232 Using whole-cell patch-clamp electrophysiology and two-photon calcium imaging, we
233 identified the sites of synaptic transmission. We detected synaptically evoked calcium transients
234 in hCO cells upon stimulation of hThOs (**Figure 3K-3N**). These postsynaptic sites in the hCO
235 cells resembled dendritic spines described in cortical neurons of animal models (**Figure 3L**).[63]
236 Stimulation of the hThO evoked stronger calcium transients in dendritic spines compared to that
237 in parent dendritic shafts (**Figure 3M** and **3N**), which suggested that the dendritic spines were
238 synaptically connected to hThO axons. Moreover, calcium transients in dendritic spines were
239 blocked by AP5 [82.4% ± 5.2% reduction (**Figure 3O**)], indicative of glutamatergic synaptic
240 transmission.

241

242 **TC and CT synapses undergo LTP in assembloids**

243 Having established the existence of functional synaptic connections between hThOs and hCOs,
244 we tested whether the TC and CT pathways undergo long-term synaptic plasticities, specifically
245 LTP and LTD. To examine whether TC synapses undergo LTP, we tested several LTP-induction
246 protocols: spike-timing–dependent plasticity (STDP) induction protocols and high-frequency
247 tetanization. TC LTP was reliably induced by high-frequency (40-Hz) tetanization of thalamic
248 inputs (**Figure 4A**), which increased EPSC amplitudes by 168.2% ± 19.3% compared to baseline
249 (**Figure 4B** and **4C**). STDP is induced by stimulating presynaptic inputs and directly depolarizing
250 the postsynaptic cell **(Figure 4D** and **4G**); STDP is based on the precise order and timing of pre-
251 and postsynaptic activity.[64–66] Following a short (×1) STDP-induction protocol, the amplitude of
252 TC EPSCs increased by 144.4% ± 17.8%, compared to baseline (**Figure 4D-4F**). Following a
253 long (×3) STDP-induction protocol, EPSC amplitudes increased by 223.9% ± 24.4%, compared
254 to baseline (**Figure 4G-4L**). This TC LTP was observed in all tested (9/9) cells, from six separate

255 assembloids, across three batches of differentiation (**Figure 4H**). TC LTP was not caused by
256 changes in series resistance (**Figure 4I**); thus, it represents a true activity-dependent potentiation
257 of synaptic strength.

258 Next, we investigated the mechanisms underlying TC LTP in assembloids. Bath
259 application of the metabotropic glutamate 5 (mGluR5) antagonist MPEP (10 μM) blocked TC LTP,
260 but the NMDAR antagonist AP5 (50 μM) did not (**Figure 4J** and **4K**). TC LTP also required
261 postsynaptic Ca^{2+}. When we included the Ca^{2+} chelator BAPTA (20 mM) in the internal pipette
262 solution (iBAPTA), the long STDP protocol not only failed to induce LTP but also moderately
263 reduced the TC EPSC amplitude (**Figure 4J** and **4K**). We then tested if TC LTP was expressed
264 presynaptically by measuring changes in PPR after LTP induction. PPR decreased (suggesting
265 an increase in the probability of glutamate release from presynaptic terminals) compared to
266 baseline in control and AP5 conditions, and this change was blocked in the presence of MPEP
267 (**Figure S7A-S7D**). Together, these findings demonstrate that the TC pathway in assembloids
268 undergoes LTP via multiple induction protocols, with the long (×3) STDP-evoked LTP induced
269 postsynaptically and expressed, at least partially, presynaptically through mGluR5-dependent
270 mechanisms.

271 CT synapses also underwent LTP after the long STDP-induction protocol (**Figure 5**). LTP
272 was observed in 12/14 cells recorded from nine separate assembloids across two differentiation
273 batches (**Figure 5B**). On average, EPSC amplitudes increased by 158.3% ± 15.2%, compared to
274 baseline after LTP induction (**Figure 5C** and **E**). CT LTP was not caused by changes in series
275 resistance (**Figure 5D**), representing a true potentiation of synaptic strength. Inclusion of iBAPTA
276 in the internal pipette solution blocked CT LTP (**Figure 5C** and **E**), and unlike TC LTP, CT LTP
277 was also blocked by separate application of MPEP and AP5 (**Figure 5C** and **E**). There were no
278 changes in PPR in any of the conditions (**Figure S7E-S7H**), suggesting that CT LTP does not
279 involve changes in presynaptic-release probabilities. These data suggest that the long (×3) STDP

280 induction protocol generates LTP in the CT pathway in assembloids, and this LTP is induced and
281 expressed postsynaptically through both mGluR5- and NMDAR-dependent mechanisms.
282
283 **TC and CT synapses undergo LTD in assembloids**
284 The activity-dependent weakening of synaptic transmission between brain regions through LTD
285 is a key component of learning.[67] Therefore, we tested whether TC and CT synapses in
286 assembloids undergo LTD. Delivering low-frequency (1-Hz) stimulation to the hThO while
287 recording from hCO cells depressed EPSCs in 8/9 cells recorded in nine assembloids from three
288 differentiation batches (**Figure 6A** and **B**). On average, TC EPSC amplitudes decreased by
289 59.4% ± 8.1% of baseline after low-frequency stimulation (**Figure 6C-6F**). TC LTD was blocked
290 by iBAPTA or bath-applied MPEP or AP5 (**Figure 6C** and **6E**). Low-frequency stimulation of the
291 hThO did not change PPR across any of the conditions (**Figure S7I-S7L**). These findings provide
292 evidence for a postsynaptically induced and expressed LTD in the TC pathway that depends on
293 both mGluR5s and NMDARs.
294 Low-frequency stimulation of hCO inputs to hThO cells also reliably induced LTD, as it
295 was observed in 10/10 cells recorded in nine assembloids across two batches of differentiation
296 (**Figure 7A** and **B**). On average, the expression of CT LTD was reflected in a 65.8% ± 5.2%
297 reduction of baseline EPSC amplitudes (**Figure 7C-7F**). CT LTD was blocked by iBAPTA or bath
298 application of MPEP or AP5 (**Figure 7C** and **7E**). PPR at CT synapses was unchanged after 1-
299 Hz stimulation across all conditions (**Figure S7M-S7P**). Neither TC LTD nor CT LTD occurred
300 due to changes in series resistance (**Figures 6D** and **7D**, respectively). These data suggest that
301 CT LTD is induced and expressed postsynaptically and requires both mGluR5s and NMDARs
302 Notably, reversing the order of presynaptic stimulation and postsynaptic depolarization, in a
303 reverse long STDP protocol, did not induce LTD in either the TC or CT pathways (data not shown).
304

305 **DISCUSSION**

306 Here we describe a novel, hiPSC-derived TC assembloid system for exploring synaptic
307 transmission and synaptic plasticity in human neural circuits. Within assembloids, hThOs and
308 hCOs form reciprocal glutamatergic synapses capable of short- and long-term synaptic plasticity.
309 Notably, the vast majority (92.9%) of synaptically connected cells underwent LTP or LTD during
310 the respective induction protocols. However, these synapses displayed a degree of specificity, as
311 one established induction protocol (reverse long STDP protocol) failed to induce LTD at either
312 synapse. Together, our findings suggest that synaptic plasticity is robust, highly replicable, and
313 selective in the TC assembloid system.

314 Previous work describing synaptic plasticity in organoids has exclusively relied on
315 multielectrode array (MEA) recordings.[68] Although this approach is high throughput and
316 convenient, MEAs measure extracellular spike and local field activities that arise from a large
317 group of cells. The specific mechanisms underlying synaptic transmission and synaptic plasticity
318 depend on pre- and postsynaptic cell identity. Neither pre- nor postsynaptic cell identities in
319 organoids are easily determined in MEA recordings because organoids contain heterogeneous
320 cell populations that lack defined electrophysiological profiles. Reflecting this heterogeneity, MEA
321 recordings in organoids detected LTP, LTD, and bidirectional short-term synaptic plasticity in
322 response to identical induction protocols.[68] Few studies have examined synaptic transmission
323 within a specific circuit in human brain organoids.[29–31] More commonly, the properties of
324 spontaneously released neurotransmitters onto single cells in organoids have been
325 characterized,[69–71] but the presynaptic sources of that transmission were not defined.

326 Our study used whole-cell patch-clamp electrophysiology, a well-validated method that
327 has enabled decades of synaptic physiology discoveries in multiple species. Here we accurately
328 measured electrically evoked synaptic currents in single postsynaptic cells. Furthermore, visually
329 differentiating between GFP^+ hCOs and GFP^- hThOs within the assembloid enabled us to evoke
330 responses from a defined neuronal population and measure changes in synaptic transmission in

distinct postsynaptic cells. To our knowledge, our results are the first to characterize functional synaptic connections and the underlying mechanisms of synaptic plasticity in a human-derived assembloid system by using these techniques.

Although there are some similarities between our LTP/LTD findings from human assembloids and those from rodents, specifically the high prevalence for NMDAR-mediated LTP and LTD,[72] in general the mechanisms underlying LTP/LTD in the rodent TC and CT pathways are distinct from what we report here.[73–75] In mouse auditory and somatosensory TC pathways, LTP depends on postsynaptically expressed group 1 mGluRs, whereas LTP in the barrel cortex requires postsynaptic NMDAR activation and subsequent Ca^{2+} entry into the postsynaptic cell.[76–80] CT LTP in rodents is expressed presynaptically, requires a rise in presynaptic Ca^{2+} and protein kinase A activation,[81] but does not require the activation of NMDARs or mGluRs[81]. In mice, LTD within the somatosensory cortex is mediated by NMDARs,[82] and LTD in the barrel cortex requires presynaptic type 1 cannabinoid receptors.[78] In contrast, we found that three of the four types of long-term synaptic plasticity we measured required both mGluR5 and NMDARs. A functional link between group 1 mGluRs and NMDAR activity is seen in various brain regions.[83,84] In mouse cortical neurons, the activation of mGluR1 potentiates NMDAR-mediated currents through downstream signaling.[85] Given our findings, a similar mGluR5-dependent mechanism may exist in human-derived TC assembloids.

Our results may reflect species-specific differences between rodents and humans in the expression and maintenance of long-term synaptic plasticity. However, organoids resemble fetal human brain more closely than they do postnatal structures,[86] and most rodent studies of synaptic physiology are conducted in postnatal animals. Unlike the adult counterparts, the immature thalamus does not contain well-differentiated nuclei, and the fetal cortical plate lacks well-defined layers. Organoids in their current forms display similar limitations in their structural organization. Therefore, the mechanisms we define in TC assembloid synaptic plasticity may differ from those

356 observed in rodents due to species differences, developmental differences, or a combination
357 thereof.

358 The organoid field is constantly improving. A recent report described hThOs that more
359 closely resemble the thalamic reticular nucleus.[87] Future studies will derive organoids that better
360 model specific projection nuclei of the thalamus. In the developing brain, thalamic inputs mold the
361 laminar, columnar, and functional organization of the cortex.[88,89] Similarly, more mature thalamic
362 projections might promote organizational maturation in hCOs, and more organized TC
363 assembloids might better model the diversity of synaptic plasticity mechanisms observed across
364 TC sensory pathways. Assembloids modeling other brain structures[90–92] (or synaptic targets
365 outside the brain)[93] might also elucidate mechanisms that differ between neural circuits.

366 We anticipate that hiPSC-derived organoids and assembloids will provide a particularly
367 useful model system for exploring synaptic pathology in human neurologic and psychiatric
368 disorders. To date, most organoid studies have focused on disease-associated changes in gene
369 expression, cellular composition, or neural network activity. Our data suggest that assembloids
370 derived from patient hiPSCs or from hiPSCs carrying disease-associated mutations can be used
371 to model disease-associated deficits in synaptic transmission and synaptic plasticity. We expect
372 that TC assembloids will be particularly useful in this respect, as functional abnormalities in many
373 thalamic nuclei are linked to psychiatric disorders, including schizophrenia.[94] The findings we
374 present here provide a foundation for those future studies.

375

REFERENCES AND NOTES

1. Ryan, T.J., and Grant, S.G.N. (2009). The origin and evolution of synapses. Preprint, 10.1038/nrn2717 10.1038/nrn2717.
2. Hensch, T.K. (2004). Critical period regulation. Annu Rev Neurosci *27*, 549–579. 10.1146/annurev.neuro.27.070203.144327.
3. Zha, C., and Sossin, W.S. (2022). The molecular diversity of plasticity mechanisms underlying memory: An evolutionary perspective. J Neurochem *163*, 444–460. 10.1111/JNC.15717.
4. Szegedi, V., Paizs, M., Csakvari, E., Molnar, G., Barzo, P., Tamas, G., and Lamsa, K. (2016). Plasticity in single axon glutamatergic connection to GABAergic interneurons regulates complex events in the human neocortex. PLoS Biol *14*. 10.1371/JOURNAL.PBIO.2000237.
5. Ataman, B., Boulting, G.L., Harmin, D.A., Yang, M.G., Baker-Salisbury, M., Yap, E.L., Malik, A.N., Mei, K., Rubin, A.A., Spiegel, I., et al. (2016). Evolution of Osteocrin as an activity-regulated factor in the primate brain. Nature *539*, 242–247. 10.1038/NATURE20111.
6. Qiu, J., McQueen, J., Bilican, B., Dando, O., Magnani, D., Punovuori, K., Selvaraj, B.T., Livesey, M., Haghi, G., Heron, S., et al. (2016). Evidence for evolutionary divergence of activity-dependent gene expression in developing neurons. Elife *5*. 10.7554/ELIFE.20337.
7. Mould, A.W., Hall, N.A., Milosevic, I., and Tunbridge, E.M. (2021). Targeting synaptic plasticity in schizophrenia: insights from genomic studies. Preprint at Elsevier Ltd, 10.1016/j.molmed.2021.07.014 10.1016/j.molmed.2021.07.014.
8. Appelbaum, L.G., Shenasa, M.A., Stolz, L., and Daskalakis, Z. (2023). Synaptic plasticity and mental health: methods, challenges and opportunities. Preprint at Springer Nature, 10.1038/s41386-022-01370-w 10.1038/s41386-022-01370-w.
9. Bourgeron, T. (2015). From the genetic architecture to synaptic plasticity in autism spectrum disorder. Preprint at Nature Publishing Group, 10.1038/nrn3992 10.1038/nrn3992.
10. Goto, Y., Yang, C.R., and Otani, S. (2010). Functional and Dysfunctional Synaptic Plasticity in Prefrontal Cortex: Roles in Psychiatric Disorders. Preprint, 10.1016/j.biopsych.2009.08.026 10.1016/j.biopsych.2009.08.026.
11. Lee, K., Park, T.I.-H., Heppner, P., Schweder, P., Mee, E.W., Dragunow, M., and Montgomery, J.M. (2020). Human in vitro systems for examining synaptic function and plasticity in the brain. J Neurophysiol *123*, 945–965. 10.1152/jn.00411.2019.
12. Kanton, S., Boyle, M.J., He, Z., Santel, M., Weigert, A., Sanchís-Calleja, F., Guijarro, P., Sidow, L., Fleck, J.S., Han, D., et al. (2019). Organoid single-cell genomic atlas uncovers human-specific features of brain development. Nature *574*, 418–422. 10.1038/S41586-019-1654-9.
13. Pollen, A.A., Bhaduri, A., Andrews, M.G., Nowakowski, T.J., Meyerson, O.S., Mostajo-Radji, M.A., Di Lullo, E., Alvarado, B., Bedolli, M., Dougherty, M.L., et al. (2019). Establishing cerebral organoids as models of human-specific brain evolution. Cell *176*, 743-756.e17. 10.1016/J.CELL.2019.01.017.
14. Agoglia, R.M., Sun, D., Birey, F., Yoon, S.J., Miura, Y., Sabatini, K., Pașca, S.P., and Fraser, H.B. (2021). Primate cell fusion disentangles gene regulatory divergence in neurodevelopment. Nature *592*, 421–427. 10.1038/S41586-021-03343-3.
15. Velasco, S., Kedaigle, A.J., Simmons, S.K., Nash, A., Rocha, M., Quadrato, G., Paulsen, B., Nguyen, L., Adiconis, X., Regev, A., et al. (2019). Individual brain organoids reproducibly form cell diversity of the human cerebral cortex. Nature *570*, 523–527. 10.1038/S41586-019-1289-X.

16. Lancaster, M.A., Renner, M., Martin, C.A., Wenzel, D., Bicknell, L.S., Hurles, M.E., Homfray, T., Penninger, J.M., Jackson, A.P., and Knoblich, J.A. (2013). Cerebral organoids model human brain development and microcephaly. Nature *501*, 373–379. 10.1038/NATURE12517.
17. Mora-Bermúdez, F., Badsha, F., Kanton, S., Camp, J.G., Vernot, B., Köhler, K., Voigt, B., Okita, K., Maricic, T., He, Z., et al. (2016). Differences and similarities between human and chimpanzee neural progenitors during cerebral cortex development. Elife *5*. 10.7554/ELIFE.18683.
18. Li, Y., Muffat, J., Omer, A., Bosch, I., Lancaster, M.A., Sur, M., Gehrke, L., Knoblich, J.A., and Jaenisch, R. (2017). Induction of expansion and folding in human cerebral organoids. Cell Stem Cell *20*, 385-396.e3. 10.1016/J.STEM.2016.11.017.
19. Li, C., Fleck, J.S., Martins-Costa, C., Burkard, T.R., Themann, J., Stuempflen, M., Peer, A.M., Vertesy, Á., Littleboy, J.B., Esk, C., et al. (2023). Single-cell brain organoid screening identifies developmental defects in autism. Nature *621*, 373–380. 10.1038/s41586-023-06473-y.
20. Wulansari, N., Darsono, W.H.W., Woo, H.-J., Chang, M.-Y., Kim, J., Bae, E.-J., Sun, W., Lee, J.-H., Cho, I.-J., Shin, H., et al. (2021). Neurodevelopmental defects and neurodegenerative phenotypes in human brain organoids carrying Parkinson's disease-linked DNAJC6 mutations. Sci Adv *7*. 10.1126/sciadv.abb1540.
21. Paulsen, B., Velasco, S., Kedaigle, A.J., Pigoni, M., Quadrato, G., Deo, A.J., Adiconis, X., Uzquiano, A., Sartore, R., Yang, S.M., et al. (2022). Autism genes converge on asynchronous development of shared neuron classes. Nature *602*, 268–273. 10.1038/s41586-021-04358-6.
22. Sebastian, R., Jin, K., Pavon, N., Bansal, R., Potter, A., Song, Y., Babu, J., Gabriel, R., Sun, Y., Aronow, B., et al. (2023). Schizophrenia-associated NRXN1 deletions induce developmental-timing- and cell-type-specific vulnerabilities in human brain organoids. Nat Commun *14*. 10.1038/s41467-023-39420-6.
23. Notaras, M., Lodhi, A., Dündar, F., Collier, P., Sayles, N.M., Tilgner, H., Greening, D., and Colak, D. (2022). Schizophrenia is defined by cell-specific neuropathology and multiple neurodevelopmental mechanisms in patient-derived cerebral organoids. Mol Psychiatry *27*, 1416–1434. 10.1038/s41380-021-01316-6.
24. Liu, C., Fu, Z., Wu, S., Wang, X., Zhang, S., Chu, C., Hong, Y., Wu, W., Chen, S., Jiang, Y., et al. (2022). Mitochondrial HSF1 triggers mitochondrial dysfunction and neurodegeneration in Huntington's disease. EMBO Mol Med *14*. 10.15252/emmm.202215851.
25. Kathuria, A., Lopez-Lengowski, K., Jagtap, S.S., McPhie, D., Perlis, R.H., Cohen, B.M., and Karmacharya, R. (2020). Transcriptomic Landscape and Functional Characterization of Induced Pluripotent Stem Cell-Derived Cerebral Organoids in Schizophrenia. JAMA Psychiatry *77*, 745–754. 10.1001/jamapsychiatry.2020.0196.
26. Magee, J.C., and Grienberger, C. (2020). Synaptic plasticity forms and functions. Annu Rev Neurosci *43*, 95–117. 10.1146/ANNUREV-NEURO-090919-022842.
27. Reha, R.K., Dias, B.G., Nelson, C.A., Kaufer, D., Werker, J.F., Kolbh, B., Levine, J.D., and Hensch, T.K. (2020). Critical period regulation across multiple timescales. Proc Natl Acad Sci U S A *117*, 23242–23251. 10.1073/PNAS.1820836117.
28. Citri, A., and Malenka, R.C. (2008). Synaptic plasticity: multiple forms, functions, and mechanisms. Neuropsychopharmacology *33*, 18–41. 10.1038/SJ.NPP.1301559.
29. Miura, Y., Li, M.-Y., Birey, F., Ikeda, K., Revah, O., Thete, M.V., Park, J.-Y., Puno, A., Lee, S.H., Porteus, M.H., et al. (2020). Generation of human striatal organoids and cortico-striatal assembloids from human pluripotent stem cells. Nat Biotechnol *38*, 1421–1430. 10.1038/s41587-020-00763-w.
30. Jo, J., Xiao, Y., Sun, A.X., Cukuroglu, E., Tran, H.D., Göke, J., Tan, Z.Y., Saw, T.Y., Tan, C.P., Lokman, H., et al. (2016). Midbrain-like Organoids from Human Pluripotent Stem

Cells Contain Functional Dopaminergic and Neuromelanin-Producing Neurons. Cell Stem Cell *19*, 248–257. 10.1016/j.stem.2016.07.005.

31. Pasca, A.M., Sloan, S.A., Clarke, L.E., Tian, Y., Makinson, C.D., Huber, N., Kim, C.H., Park, J.Y., O'Rourke, N.A., Nguyen, K.D., et al. (2015). Functional cortical neurons and astrocytes from human pluripotent stem cells in 3D culture. Nat Methods *12*, 671–678. 10.1038/nmeth.3415.
32. Xiang, Y., Tanaka, Y., Cakir, B., Patterson, B., Kim, K.-Y., Sun, P., Kang, Y.-J., Zhong, M., Liu, X., Patra, P., et al. (2019). hESC-derived thalamic organoids form reciprocal projections when fused with cortical organoids. Cell Stem Cell *24*, 487-497.e7. 10.1016/j.stem.2018.12.015.
33. Abramson, B.P., and Chalupa, L.M. (1985). The laminar distribution of cortical connections with the tecto- and cortico-recipient zones in the cat's lateral posterior nucleus. Neuroscience *15*, 81–95. 10.1016/0306-4522(85)90125-3.
34. Rockland, K.S., Andresen, J., Cowie, R.J., and Robinson, D.L. (1999). Single axon analysis of pulvinocortical connections to several visual areas in the Macaque. J Comp Neurol *406*, 221–250. 10.1002/(SICI)1096-9861(19990405)406:2<221::AID-CNE7>3.0.CO;2-K.
35. Halassa, M.M., and Sherman, S.M. (2019). Thalamocortical circuit motifs: a general framework. Neuron *103*, 762–770. 10.1016/j.neuron.2019.06.005.
36. Nakajima, M., and Halassa, M.M. (2017). Thalamic control of functional cortical connectivity. Curr Opin Neurobiol *44*, 127–131. 10.1016/j.conb.2017.04.001.
37. Briggs, F., and Usrey, W.M. (2008). Emerging views of corticothalamic function. Curr Opin Neurobiol *18*, 403–407. 10.1016/J.CONB.2008.09.002.
38. Sherman, S.M. (2016). Thalamus plays a central role in ongoing cortical functioning. Nat Neurosci *19*, 533–541. 10.1038/NN.4269.
39. Takahashi, N., Moberg, S., Zolnik, T.A., Catanese, J., Sachdev, R.N.S., Larkum, M.E., and Jaeger, D. (2021). Thalamic input to motor cortex facilitates goal-directed action initiation. Curr Biol *31*, 4148-4155.e4. 10.1016/J.CUB.2021.06.089.
40. Hwang, K., Shine, J.M., Cole, M.W., and Sorenson, E. (2022). Thalamocortical contributions to cognitive task activity. Elife *11*. 10.7554/ELIFE.81282.
41. Saalmann, Y.B., Pinsk, M.A., Wang, L., Li, X., and Kastner, S. (2012). The pulvinar regulates information transmission between cortical areas based on attention demands. Science *337*, 753–756. 10.1126/SCIENCE.1223082.
42. Wimmer, R.D., Schmitt, L.I., Davidson, T.J., Nakajima, M., Deisseroth, K., and Halassa, M.M. (2015). Thalamic control of sensory selection in divided attention. Nature *526*, 705–709. 10.1038/NATURE15398.
43. Biane, J.S., Takashima, Y., Scanziani, M., Conner, J.M., and Tuszynski, M.H. (2016). Thalamocortical projections onto behaviorally relevant neurons exhibit plasticity during adult motor learning. Neuron *89*, 1173–1179. 10.1016/J.NEURON.2016.02.001.
44. Audette, N.J., Bernhard, S.M., Ray, A., Stewart, L.T., and Barth, A.L. (2019). Rapid plasticity of higher-order thalamocortical inputs during sensory learning. Neuron *103*, 277-291.e4. 10.1016/J.NEURON.2019.04.037.
45. Scott, G.A., Liu, M.C., Tahir, N.B., Zabder, N.K., Song, Y., Greba, Q., and Howland, J.G. (2020). Roles of the medial prefrontal cortex, mediodorsal thalamus, and their combined circuit for performance of the odor span task in rats: analysis of memory capacity and foraging behavior. Learn Mem *27*, 67–77. 10.1101/LM.050195.119.
46. Phillips, J.M., Kambi, N.A., Redinbaugh, M.J., Mohanta, S., and Saalmann, Y.B. (2021). Disentangling the influences of multiple thalamic nuclei on prefrontal cortex and cognitive control. Neurosci Biobehav Rev *128*, 487–510. 10.1016/J.NEUBIOREV.2021.06.042.
47. Blundon, J.A., Roy, N.C., Teubner, B.J.W., Yu, J., Eom, T.-Y., Sample, K.J.J., Pani, A., Smeyne, R.J., Han, S.B., Kerekes, R.A., et al. (2017). Restoring auditory cortex plasticity

529 in adult mice by restricting thalamic adenosine signaling. Science *356*, 1352–1356.
530 10.1126/science.aaf4612.
531 48. Vue, T.Y., Aaker, J., Taniguchi, A., Kazemzadeh, C., Skidmore, J.M., Martin, D.M.,
532 Martin, J.F., Treier, M., and Nakagawa, Y. (2007). Characterization of progenitor domains
533 in the developing mouse thalamus. J Comp Neurol *505*, 73–91. 10.1002/cne.21467.
534 49. Rai, M., Coleman, Z., Curley, M., Nityanandam, A., Platt, A., Robles-Murguia, M., Jiao, J.,
535 Finkelstein, D., Wang, Y.D., Xu, B., et al. (2021). Proteasome stress in skeletal muscle
536 mounts a long-range protective response that delays retinal and brain aging. *33*, 1137-
537 1154.e9. 10.1016/J.CMET.2021.03.005.
538 50. Herrmann, K., Antonini, A., and Shatz, C.J. (1994). Ultrastructural evidence for synaptic
539 interactions between thalamocortical axons and subplate neurons. European Journal of
540 Neuroscience *6*, 1729–1742. 10.1111/j.1460-9568.1994.tb00565.x.
541 51. Polioudakis, D., de la Torre-Ubieta, L., Langerman, J., Elkins, A.G., Shi, X., Stein, J.L.,
542 Vuong, C.K., Nichterwitz, S., Gevorgian, M., Opland, C.K., et al. (2019). A single-cell
543 transcriptomic atlas of human neocortical development during mid-gestation. Neuron *103*,
544 785-801.e8. 10.1016/j.neuron.2019.06.011.
545 52. Kanold, P.O., and Luhmann, H.J. (2010). The subplate and early cortical circuits. Annu
546 Rev Neurosci *33*, 23–48. 10.1146/annurev-neuro-060909-153244.
547 53. De Gois, S., Schäfer, M.K.-H., Defamie, N., Chen, C., Ricci, A., Weihe, E., Varoqui, H.,
548 and Erickson, J.D. (2005). Homeostatic scaling of vesicular glutamate and GABA
549 transporter expression in rat neocortical circuits. The Journal of Neuroscience *25*, 7121–
550 7133. 10.1523/JNEUROSCI.5221-04.2005.
551 54. Zhang, Q., Lee, W.-C.A., Paul, D.L., and Ginty, D.D. (2019). Multiplexed peroxidase-
552 based electron microscopy labeling enables simultaneous visualization of multiple cell
553 types. Nat Neurosci *22*, 828–839. 10.1038/s41593-019-0358-7.
554 55. Beierlein, M., and Connors, B.W. (2002). Short-term dynamics of thalamocortical and
555 intracortical synapses onto layer 6 neurons in neocortex. J Neurophysiol *88*, 1924–1932.
556 56. Rose, H.J., and Metherate, R. (2005). Auditory thalamocortical transmission is reliable
557 and temporally precise. J.Neurophysiol. *94*, 2019–2030.
558 57. Bayazitov, I.T., Westmoreland, J.J., and Zakharenko, S.S. (2013). Forward suppression
559 in the auditory cortex is caused by the Ca3.1 calcium channel-mediated switch from
560 bursting to tonic firing at thalamocortical projections. Journal of Neuroscience *33*, 18940–
561 18950. 10.1523/JNEUROSCI.3335-13.2013.
562 58. Viaene, A.N., Petrof, I., and Sherman, S.M. (2011). Properties of the thalamic projection
563 from the posterior medial nucleus to primary and secondary somatosensory cortices in
564 the mouse. Proc Natl Acad Sci U S A *108*, 18156–18161. 10.1073/pnas.1114828108.
565 59. Gil, Z., Connors, B.W., and Amitai, Y. (1999). Efficacy of thalamocortical and intracortical
566 synaptic connections: quanta, innervation, and reliability. Neuron *23*, 385–397.
567 60. Stratford, K.J., Tarczy-Hornoch, K., Martin, K.A., Bannister, N.J., and Jack, J.J. (1996).
568 Excitatory synaptic inputs to spiny stellate cells in cat visual cortex. Nature *382*, 258–261.
569 61. Beierlein, M., Fall, C.P., Rinzel, J., and Yuste, R. (2002). Thalamocortical bursts trigger
570 recurrent activity in neocortical networks: layer 4 as a frequency-dependent gate. J
571 Neurosci *22*, 9885–9894.
572 62. Zhao, W., Johnston, K.G., Ren, H., Xu, X., and Nie, Q. (2023). Inferring neuron-neuron
573 communications from single-cell transcriptomics through NeuronChat. Nat Commun *14*.
574 10.1038/s41467-023-36800-w.
575 63. Richardson, R.J., Blundon, J.A., Bayazitov, I.T., and Zakharenko, S.S. (2009).
576 Connectivity patterns revealed by mapping of active inputs on dendrites of
577 thalamorecipient neurons in the auditory cortex. Journal of Neuroscience *29*, 6406–6417.
578 10.1523/JNEUROSCI.0258-09.2009.
579 64. Debanne, D., and Inglebert, Y. (2023). Spike timing-dependent plasticity and memory.
580 Curr Opin Neurobiol *80*, 102707. 10.1016/j.conb.2023.102707.

65. Feldman, D.E. (2012). The spike-timing dependence of plasticity. Neuron *75*, 556–571. 10.1016/j.neuron.2012.08.001.
66. Dan, Y., and Poo, M.M. (2004). Spike timing-dependent plasticity of neural circuits. Neuron *44*, 23–30.
67. Collingridge, G.L., Peineau, S., Howland, J.G., and Wang, Y.T. (2010). Long-term depression in the CNS. Nat.Rev.Neurosci *11*, 459–473. 10.1038/NRN2867.
68. Zafeiriou, M.P., Bao, G., Hudson, J., Halder, R., Blenkle, A., Schreiber, M.K., Fischer, A., Schild, D., and Zimmermann, W.H. (2020). Developmental GABA polarity switch and neuronal plasticity in Bioengineered Neuronal Organoids. Nat Commun *11*. 10.1038/s41467-020-17521-w.
69. Muguruma, K., Nishiyama, A., Kawakami, H., Hashimoto, K., and Sasai, Y. (2015). Self-organization of polarized cerebellar tissue in 3D culture of human pluripotent stem cells. Cell Rep *10*, 537–550. 10.1016/j.celrep.2014.12.051.
70. Sakaguchi, H., Kadoshima, T., Soen, M., Narii, N., Ishida, Y., Ohgushi, M., Takahashi, J., Eiraku, M., and Sasai, Y. (2015). Generation of functional hippocampal neurons from self-organizing human embryonic stem cell-derived dorsomedial telencephalic tissue. Nat Commun *6*. 10.1038/ncomms9896.
71. Mariani, J., Coppola, G., Zhang, P., Abyzov, A., Provini, L., Tomasini, L., Amenduni, M., Szekely, A., Palejev, D., Wilson, M., et al. (2015). FOXG1-Dependent Dysregulation of GABA/Glutamate Neuron Differentiation in Autism Spectrum Disorders. Cell *162*, 375–390. 10.1016/j.cell.2015.06.034.
72. Lüscher, C., and Malenka, R.C. (2012). NMDA receptor-dependent long-term potentiation and long-term depression (LTP/LTD). Cold Spring Harb Perspect Biol *4*. 10.1101/cshperspect.a005710.
73. Pisani, A., Gubellini, P., Bonsi, P., Conquet, F., Picconi, B., Centonze, D., Bernardi, G., and Calabresi, P. (2001). Metabotropic glutamate receptor 5 mediates the potentiation of N-methyl-D-aspartate responses in medium spiny striatal neurons. Neuroscience *106*, 579–587. 10.1016/s0306-4522(01)00297-4.
74. Benquet, P., Gee, C.E., and Gerber, U. (2002). Two distinct signaling pathways upregulate NMDA receptor responses via two distinct metabotropic glutamate receptor subtypes. J Neurosci *22*, 9679–9686. 10.1523/JNEUROSCI.22-22-09679.2002.
75. Heidinger, V., Manzerra, P., Wang, X.Q., Strasser, U., Yu, S.-P., Choi, D.W., and Behrens, M.M. (2002). Metabotropic glutamate receptor 1-induced upregulation of NMDA receptor current: mediation through the Pyk2/Src-family kinase pathway in cortical neurons. J Neurosci *22*, 5452–5461. 10.1523/JNEUROSCI.22-13-05452.2002.
76. Fox, K., Schlaggar, B.L., Glazewski, S., and O'Leary, D.D. (1996). Glutamate receptor blockade at cortical synapses disrupts development of thalamocortical and columnar organization in somatosensory cortex. Proc Natl Acad Sci U S A *93*, 5584–5589. 10.1073/pnas.93.11.5584.
77. Schlaggar, B.L., Fox, K., and O'Leary, D.D. (1993). Postsynaptic control of plasticity in developing somatosensory cortex. Nature *364*, 623–626. 10.1038/364623a0.
78. Itami, C., Huang, J.-Y., Yamasaki, M., Watanabe, M., Lu, H.-C., and Kimura, F. (2016). Developmental switch in spike timing-dependent plasticity and cannabinoid-dependent reorganization of the thalamocortical projection in the barrel Cortex. J Neurosci *36*, 7039–7054. 10.1523/JNEUROSCI.4280-15.2016.
79. Crair, M.C., and Malenka, R.C. (1995). A critical period for long-term potentiation at thalamocortical synapses. Nature *375*, 325–328. 10.1038/375325a0.
80. Chun, S., Bayazitov, I.T., Blundon, J.A., and Zakharenko, S.S. (2013). Thalamocortical long-term potentiation becomes gated after the early critical period in the auditory cortex. Journal of Neuroscience *33*, 7345–7357. 10.1523/JNEUROSCI.4500-12.2013.

81. Castro-Alamancos, M.A., and Calcagnotto, M.E. (1999). Presynaptic long-term potentiation in corticothalamic synapses. J Neurosci *19*, 9090–9097. 10.1523/JNEUROSCI.19-20-09090.1999.
82. Feldman, D.E., Nicoll, R.A., Malenka, R.C., and Isaac, J.T. (1998). Long-term depression at thalamocortical synapses in developing rat somatosensory cortex. Neuron *21*, 347–357. 10.1016/s0896-6273(00)80544-9.
83. Pisani, A., Gubellini, P., Bonsi, P., Conquet, F., Picconi, B., Centonze, D., Bernardi, G., and Calabresi, P. (2001). Metabotropic glutamate receptor 5 mediates the potentiation of N-methyl-D-aspartate responses in medium spiny striatal neurons. Neuroscience *106*, 579–587. 10.1016/s0306-4522(01)00297-4.
84. Benquet, P., Gee, C.E., and Gerber, U. (2002). Two distinct signaling pathways upregulate NMDA receptor responses via two distinct metabotropic glutamate receptor subtypes. J Neurosci *22*, 9679–9686. 10.1523/JNEUROSCI.22-22-09679.2002.
85. Heidinger, V., Manzerra, P., Wang, X.Q., Strasser, U., Yu, S.-P., Choi, D.W., and Behrens, M.M. (2002). Metabotropic glutamate receptor 1-induced upregulation of NMDA receptor current: mediation through the Pyk2/Src-family kinase pathway in cortical neurons. J Neurosci *22*, 5452–5461. 10.1523/JNEUROSCI.22-13-05452.2002.
86. Amiri, A., Coppola, G., Scuderi, S., Wu, F., Roychowdhury, T., Liu, F., Pochareddy, S., Shin, Y., Safi, A., Song, L., et al. (2018). Transcriptome and epigenome landscape of human cortical development modeled in organoids. Science *362*. 10.1126/science.aat6720.
87. Kiral, F.R., Cakir, B., Tanaka, Y., Kim, J., Yang, W.S., Wehbe, F., Kang, Y.-J., Zhong, M., Sancer, G., Lee, S.-H., et al. (2023). Generation of ventralized human thalamic organoids with thalamic reticular nucleus. Cell Stem Cell *30*, 677-688.e5. 10.1016/j.stem.2023.03.007.
88. Monko, T., Rebertus, J., Stolley, J., Salton, S.R., and Nakagawa, Y. (2022). Thalamocortical axons regulate neurogenesis and laminar fates in the early sensory cortex. Proc Natl Acad Sci U S A *119*, e2201355119. 10.1073/pnas.2201355119.
89. Antón-Bolaños, N., Sempere-Ferràndez, A., Guillamón-Vivancos, T., Martini, F.J., Pérez-Saiz, L., Gezelius, H., Filipchuk, A., Valdeolmillos, M., and López-Bendito, G. (2019). Prenatal activity from thalamic neurons governs the emergence of functional cortical maps in mice. Science *364*, 987–990. 10.1126/science.aav7617.
90. Miura, Y., Li, M.-Y., Birey, F., Ikeda, K., Revah, O., Thete, M.V., Park, J.-Y., Puno, A., Lee, S.H., Porteus, M.H., et al. (2020). Generation of human striatal organoids and cortico-striatal assembloids from human pluripotent stem cells. Nat Biotechnol *38*, 1421–1430. 10.1038/s41587-020-00763-w.
91. Birey, F., Andersen, J., Makinson, C.D., Islam, S., Wei, W., Huber, N., Fan, H.C., Metzler, K.R.C., Panagiotakos, G., Thom, N., et al. (2017). Assembly of functionally integrated human forebrain spheroids. Nature *545*, 54–59. 10.1038/nature22330.
92. Bagley, J.A., Reumann, D., Bian, S., Lévi-Strauss, J., and Knoblich, J.A. (2017). Fused cerebral organoids model interactions between brain regions. Nat Methods *14*, 743–751. 10.1038/nmeth.4304.
93. Andersen, J., Revah, O., Miura, Y., Thom, N., Amin, N.D., Kelley, K.W., Singh, M., Chen, X., Thete, M.V., Walczak, E.M., et al. (2020). Generation of functional human 3D cortico-motor assembloids. Cell *183*, 1913-1929.e26. 10.1016/j.cell.2020.11.017.
94. Jiang, Y., Patton, M.H., and Zakharenko, S.S. (2021). A case for thalamic mechanisms of schizophrenia: perspective from modeling 22q11.2 deletion syndrome. Front Neural Circuits *15*. 10.3389/fncir.2021.769969.
95. Sloan, S.A., Darmanis, S., Huber, N., Khan, T.A., Birey, F., Caneda, C., Reimer, R., Quake, S.R., Barres, B.A., and Paşca, S.P. (2017). Human astrocyte maturation captured in 3D cerebral cortical spheroids derived from pluripotent stem cells. Neuron *95*, 779-790.e6. 10.1016/j.neuron.2017.07.035.

683 96. Tsankov, A.M., Akopian, V., Pop, R., Chetty, S., Gifford, C.A., Daheron, L., Tsankova,
684 N.M., and Meissner, A. (2015). A qPCR ScoreCard quantifies the differentiation potential
685 of human pluripotent stem cells. Nat Biotechnol *33*, 1182–1192. 10.1038/nbt.3387.
686 97. Assou, S., Girault, N., Plinet, M., Bouckenheimer, J., Sansac, C., Combe, M., Mianné, J.,
687 Bourguignon, C., Fieldes, M., Ahmed, E., et al. (2020). Recurrent genetic abnormalities in
688 human pluripotent stem cells: definition and routine detection in culture supernatant by
689 targeted droplet digital PCR. Stem Cell Reports *14*, 1–8. 10.1016/j.stemcr.2019.12.004.
690 98. Baker, D., Hirst, A.J., Gokhale, P.J., Juarez, M.A., Williams, S., Wheeler, M., Bean, K.,
691 Allison, T.F., Moore, H.D., Andrews, P.W., et al. (2016). Detecting genetic mosaicism in
692 cultures of human pluripotent stem cells. Stem Cell Reports *7*, 998–1012.
693 10.1016/j.stemcr.2016.10.003.
694 99. Martins-Taylor, K., Nisler, B.S., Taapken, S.M., Compton, T., Crandall, L., Montgomery,
695 K.D., Lalande, M., and Xu, R.-H. (2011). Recurrent copy number variations in human
696 induced pluripotent stem cells. Nat Biotechnol *29*, 488–491. 10.1038/nbt.1890.
697 100. Nishino, K., Toyoda, M., Yamazaki-Inoue, M., Fukawatase, Y., Chikazawa, E.,
698 Sakaguchi, H., Akutsu, H., and Umezawa, A. (2011). DNA methylation dynamics in
699 human induced pluripotent stem cells over time. PLoS Genet *7*, e1002085.
700 10.1371/journal.pgen.1002085.
701 101. Johannesson, B., Sagi, I., Gore, A., Paull, D., Yamada, M., Golan-Lev, T., Li, Z., LeDuc,
702 C., Shen, Y., Stern, S., et al. (2014). Comparable frequencies of coding mutations and
703 loss of imprinting in human pluripotent cells derived by nuclear transfer and defined
704 factors. Cell Stem Cell *15*, 634–642. 10.1016/j.stem.2014.10.002.
705 102. Norrie, J.L., Nityanandam, A., Lai, K., Chen, X., Wilson, M., Stewart, E., Griffiths, L., Jin,
706 H., Wu, G., Orr, B., et al. (2021). Retinoblastoma from human stem cell-derived retinal
707 organoids. Nat Commun *12*, 4535. 10.1038/s41467-021-24781-7.
708 103. Sentmanat, M.F., Peters, S.T., Florian, C.P., Connelly, J.P., and Pruett-Miller, S.M.
709 (2018). A survey of validation strategies for CRISPR-Cas9 editing. Sci Rep *8*, 888.
710 10.1038/s41598-018-19441-8.
711 104. Connelly, J.P., and Pruett-Miller, S.M. (2019). CRIS.py: a versatile and high-throughput
712 analysis program for CRISPR-based genome editing. Sci Rep *9*, 4194.
713 doi.org/10.1038/s41598-019-40896-w.
714 105. Chen, Y., Tristan, C.A., Chen, L., Jovanovic, V.M., Malley, C., Chu, P.-H., Ryu, S., Deng,
715 T., Ormanoglu, P., Tao, D., et al. (2021). A versatile polypharmacology platform promotes
716 cytoprotection and viability of human pluripotent and differentiated cells. Nat Methods *18*,
717 528–541. 10.1038/s41592-021-01126-2.
718 106. Keaveney, M.K., Tseng, H.-A., Ta, T.L., Gritton, H.J., Man, H.-Y., and Han, X. (2018). A
719 microRNA-based gene-targeting tool for virally labeling interneurons in the rodent cortex.
720 Cell Rep *24*, 294–303. 10.1016/j.celrep.2018.06.049.
721 107. Miller, J.D., Ganat, Y.M., Kishinevsky, S., Bowman, R.L., Liu, B., Tu, E.Y., Mandal, P.K.,
722 Vera, E., Shim, J., Kriks, S., et al. (2013). Human iPSC-based modeling of late-onset
723 disease via progerin-induced aging. Cell Stem Cell *13*, 691–705.
724 10.1016/j.stem.2013.11.006.
725 108. Dobin, A., Davis, C.A., Schlesinger, F., Drenkow, J., Zaleski, C., Jha, S., Batut, P.,
726 Chaisson, M., and Gingeras, T.R. (2013). STAR: ultrafast universal RNA-seq aligner.
727 Bioinformatics *29*, 15–21. 10.1093/bioinformatics/bts635.
728 109. Li, B., and Dewey, C.N. (2011). RSEM: accurate transcript quantification from RNA-Seq
729 data with or without a reference genome. BMC Bioinformatics *12*, 323. 10.1186/1471-
730 2105-12-323.
731 110. Robinson, M.D., McCarthy, D.J., and Smyth, G.K. (2010). edgeR: a Bioconductor
732 package for differential expression analysis of digital gene expression data.
733 Bioinformatics *26*, 139–140. 10.1093/bioinformatics/btp616.

111. Ritchie, M.E., Phipson, B., Wu, D., Hu, Y., Law, C.W., Shi, W., and Smyth, G.K. (2015). limma powers differential expression analyses for RNA-sequencing and microarray studies. Nucleic Acids Res *43*, e47. 10.1093/nar/gkv007.
112. Fleck, J.S., Sanchís-Calleja, F., He, Z., Santel, M., Boyle, M.J., Camp, J.G., and Treutlein, B. (2021). Resolving organoid brain region identities by mapping single-cell genomic data to reference atlases. Cell Stem Cell *28*, 1148-1159.e8. 10.1016/j.stem.2021.02.015.
113. Raudvere, U., Kolberg, L., Kuzmin, I., Arak, T., Adler, P., Peterson, H., and Vilo, J. (2019). g:Profiler: a web server for functional enrichment analysis and conversions of gene lists (2019 update). Nucleic Acids Res *47*, W191–W198. 10.1093/NAR/GKZ369.
114. Wickham, H. (2016). ggplot2: Elegant Graphics for Data Analysis (Springer-Verlag New York).
115. Gu, Z., Eils, R., and Schlesner, M. (2016). Complex heatmaps reveal patterns and correlations in multidimensional genomic data. Bioinformatics *32*, 2847–2849. 10.1093/bioinformatics/btw313.
116. Gu, Z. (2022). Complex heatmap visualization. iMeta *1*. 10.1002/imt2.43.
117. Livak, K.J., and Schmittgen, T.D. (2001). Analysis of relative gene expression data using real-time quantitative PCR and the 2(-Delta Delta C(T)) Method. Methods *25*, 402–408. 10.1006/meth.2001.1262.
118. Matson, K.J.E., Sathyamurthy, A., Johnson, K.R., Kelly, M.C., Kelley, M.W., and Levine, A.J. (2018). Isolation of adult spinal cord nuclei for massively parallel single-nucleus RNA sequencing. J Vis Exp. 10.3791/58413.
119. Young, M.D., and Behjati, S. (2020). SoupX removes ambient RNA contamination from droplet-based single-cell RNA sequencing data. Gigascience *9*. 10.1093/gigascience/giaa151.
120. Hao, Y., Hao, S., Andersen-Nissen, E., Mauck, W.M., Zheng, S., Butler, A., Lee, M.J., Wilk, A.J., Darby, C., Zager, M., et al. (2021). Integrated analysis of multimodal single-cell data. Cell *184*, 3573-3587.e29. 10.1016/j.cell.2021.04.048.
121. Stuart, T., Butler, A., Hoffman, P., Hafemeister, C., Papalexi, E., Mauck, W.M., Hao, Y., Stoeckius, M., Smibert, P., and Satija, R. (2019). Comprehensive integration of single-cell data. Cell *177*, 1888-1902.e21. 10.1016/j.cell.2019.05.031.
122. Butler, A., Hoffman, P., Smibert, P., Papalexi, E., and Satija, R. (2018). Integrating single-cell transcriptomic data across different conditions, technologies, and species. Nat Biotechnol *36*, 411–420. 10.1038/nbt.4096.
123. Satija, R., Farrell, J.A., Gennert, D., Schier, A.F., and Regev, A. (2015). Spatial reconstruction of single-cell gene expression data. Nat Biotechnol *33*, 495–502. 10.1038/nbt.3192.
124. Tirosh, I., Izar, B., Prakadan, S.M., Wadsworth, M.H., Treacy, D., Trombetta, J.J., Rotem, A., Rodman, C., Lian, C., Murphy, G., et al. (2016). Dissecting the multicellular ecosystem of metastatic melanoma by single-cell RNA-seq. Science *352*, 189–196. 10.1126/science.aad0501.
125. Korsunsky, I., Millard, N., Fan, J., Slowikowski, K., Zhang, F., Wei, K., Baglaenko, Y., Brenner, M., Loh, P.-R., and Raychaudhuri, S. (2019). Fast, sensitive and accurate integration of single-cell data with Harmony. Nat Methods *16*, 1289–1296. 10.1038/s41592-019-0619-0.
126. Trapnell, C., Cacchiarelli, D., Grimsby, J., Pokharel, P., Li, S., Morse, M., Lennon, N.J., Livak, K.J., Mikkelsen, T.S., and Rinn, J.L. (2014). The dynamics and regulators of cell fate decisions are revealed by pseudotemporal ordering of single cells. Nat Biotechnol *32*, 381–386. 10.1038/nbt.2859.
127. Qiu, X., Mao, Q., Tang, Y., Wang, L., Chawla, R., Pliner, H.A., and Trapnell, C. (2017). Reversed graph embedding resolves complex single-cell trajectories. Nat Methods *14*, 979–982. 10.1038/nmeth.4402.

786 128. Qiu, X., Hill, A., Packer, J., Lin, D., Ma, Y.-A., and Trapnell, C. (2017). Single-cell mRNA
787 quantification and differential analysis with Census. Nat Methods *14*, 309–315.
788 10.1038/nmeth.4150.
789 129. Cao, J., Spielmann, M., Qiu, X., Huang, X., Ibrahim, D.M., Hill, A.J., Zhang, F., Mundlos,
790 S., Christiansen, L., Steemers, F.J., et al. (2019). The single-cell transcriptional
791 landscape of mammalian organogenesis. Nature *566*, 496–502. 10.1038/s41586-019-
792 0969-x.
793 130. Govek, K.W., Chen, S., Sgourdou, P., Yao, Y., Woodhouse, S., Chen, T., Fuccillo, M. V,
794 Epstein, D.J., and Camara, P.G. (2022). Developmental trajectories of thalamic
795 progenitors revealed by single-cell transcriptome profiling and Shh perturbation. Cell Rep
796 *41*, 111768. 10.1016/j.celrep.2022.111768.
797 131. Guo, Q., and Li, J.Y.H. (2019). Defining developmental diversification of diencephalon
798 neurons through single cell gene expression profiling. Development *146*.
799 10.1242/dev.174284.
800 132. Vue, T.Y., Aaker, J., Taniguchi, A., Kazemzadeh, C., Skidmore, J.M., Martin, D.M.,
801 Martin, J.F., Treier, M., and Nakagawa, Y. (2007). Characterization of progenitor domains
802 in the developing mouse thalamus. J Comp Neurol *505*, 73–91. 10.1002/cne.21467.
803 133. Martell, J.D., Deerinck, T.J., Lam, S.S., Ellisman, M.H., and Ting, A.Y. (2017). Electron
804 microscopy using the genetically encoded APEX2 tag in cultured mammalian cells. Nat
805 Protoc *12*, 1792–1816. 10.1038/nprot.2017.065.
806 134. Garad, M., Edelmann, E., and Leßmann, V. (2021). Impairment of spike-timing-
807 dependent plasticity at Schaffer collateral-CA1 synapses in adult APP/PS1 mice depends
808 on proximity of Aβ plaques. Int J Mol Sci *22*. 10.3390/ijms22031378.
809 135. Blundon, J.A., Bayazitov, I.T., and Zakharenko, S.S. (2011). Presynaptic gating of
810 postsynaptically expressed plasticity at mature thalamocortical synapses. Journal of
811 Neuroscience *31*, 16012–16025. 10.1523/JNEUROSCI.3281-11.2011.
812

813

814 **Acknowledgments:** We thank Yiping Fan, Dale Hedges, and Daniel Estevez Prado (St. Jude
815 Center for Applied Bioinformatics, Transcriptomics Group) for assistance with bulk RNA-seq data
816 analysis; Lawrence Reiter for providing the TP-190a and TP-189 dental pulp stem cells for
817 reprogramming; Sergiu Pasca for providing the 2242, 1205, and 8858 hiPSC lines; Angela
818 McArthur for manuscript editing; and Zakharenko lab members for constructive comments.

819

820 **Funding:** This work was funded, in part, by the National Institutes of Health grants R01
821 MH097742 and R01 DC012833 (to SSZ), K99 MH129617 (to MHP), the Stanford Maternal and
822 Child Health Research Institute Uytengsu-Hamilton 22q11 Neuropsychiatry Research Program
823 grants UH22QEXTFY21 and UH22QEXTFY23 (to SSZ), the National Cancer Institute grant P30
824 CA021765, and the American Lebanese Syrian Associated Charities (ALSAC). The content is
825 solely the responsibility of the authors and does not necessarily represent the official views of
826 the National Institutes of Health or other granting agencies.

827

828 **Author contributions:**

829 Conceptualization: MHP, KTT, SSZ

830 Electrophysiology experiments: MHP, ITB, YJ

831 Molecular biology experiments: KTT, AN, ABS

832 Two-photon imaging experiments: ITB

833 hiPSC line maintenance, organoid differentiation, and assembloid preparation: AN, KDN

834 Electron microscopy: NBK, CGR

835 snRNA-seq sample preparation: AJT, JBB

836 snRNA-seq data analysis: CAR, KTT

837 Design and production of hiPSC reporter lines: STP, SMP-M

838 Visualization: MHP, KTT

839 Funding acquisition: SSZ

840 Supervision: SSZ

841 Writing – original draft: MHP, KTT

842 Writing – review & editing: SSZ

843

844 **Competing interests:** The authors declare no competing interests.

845

846 **Data and materials availability:** The snRNA-seq data that support the findings of this study
847 have been deposited in SRA under the Bioproject ID PRJNA999219. Bulk RNA-seq data have
848 been deposited in SRA under Bioproject ID PRJNA1001283. Code used for the analysis of
849 snRNA-seq data is available at Github
850 (https://github.com/ZakharenkoLab/Thalamic_and_Cortical_Organoid_snRNASeq). Additional R
851 code is available upon request.

852

853 **Supplemental Materials**

854 Figures S1 to S7

855 Table S1

856

Figures

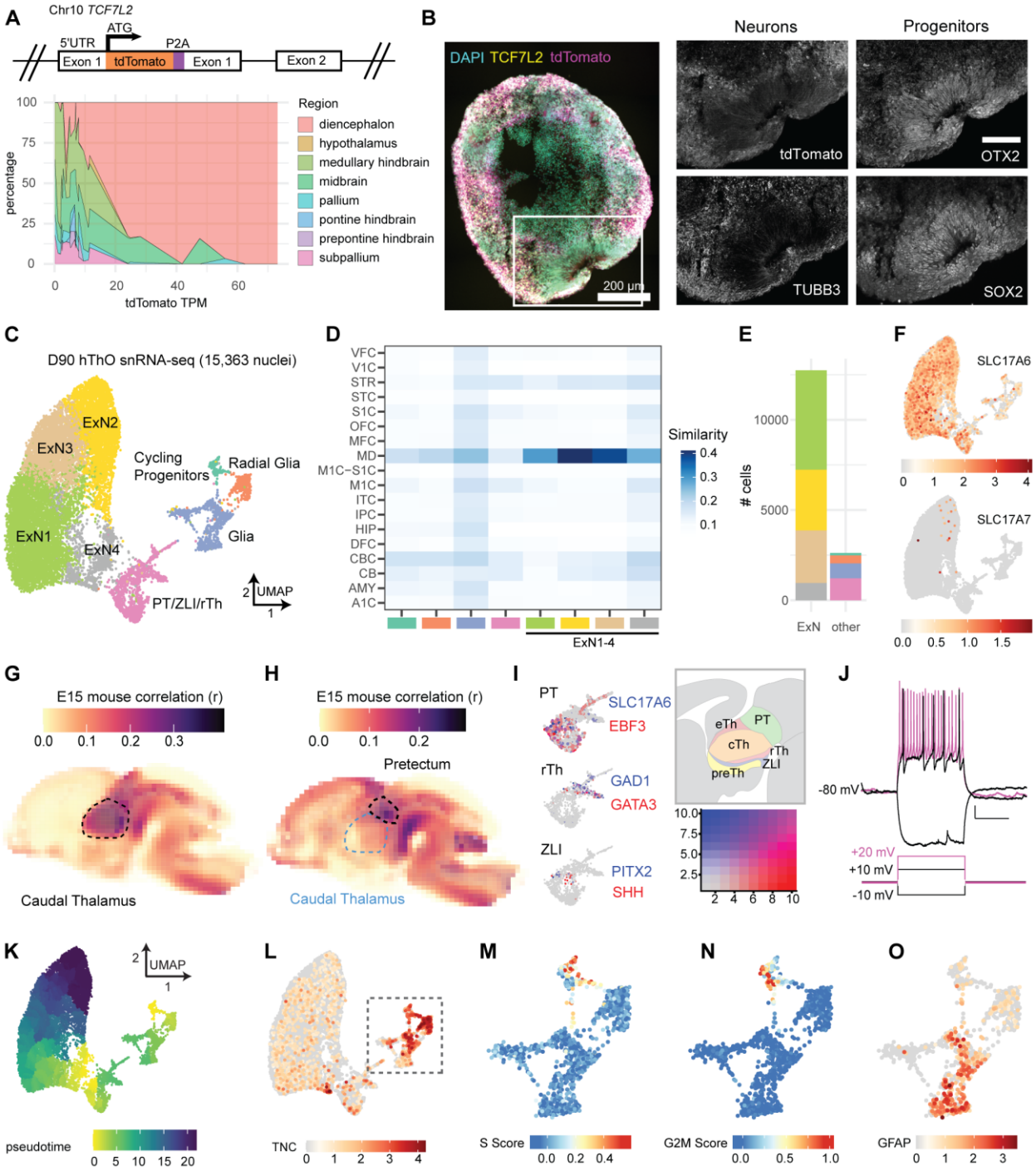

Figure 1. hThOs contain functional glutamatergic thalamic neurons.
(**A**) Reporter cell line validation for hThOs. Top: Schematic of *TCF7L2* exon 1 in the TP-190a-TCF7L2-tdTomato reporter line, which was used to generate all hThOs, except where indicated in Figure S2. Bottom: VoxHunt deconvolution analysis of bulk RNA-seq data from D69-D70 hThOs using E13 mouse brain data from the *Allen Brain Atlas* as a reference.
(**B**) Immunofluorescence images of TCF7L2, TUBB3, OTX2, and SOX2 labeling in D60 hThOs. Nuclei are indicated by DAPI (cyan). TCF7L2-tdTomato fluorescence is indicated in magenta.

866 Images were acquired from serial sections of the same organoid. Scale bars: 200 µm (whole
867 section), 100 µm (insets).
868 (**C**) UMAP plot with cluster annotations indicated by color.
869 (**D**) VoxHunt analysis by snRNA-seq cell cluster. Excitatory neuron (ExN) clusters exhibit the
870 highest correlations with *BrainSpan* samples from human mediodorsal nucleus of the thalamus
871 (MD), aged 13–24 pcw. Cluster annotations are indicated by color on the x-axis.
872 (**E**) Bar plot showing the number of nuclei per cell cluster, with clusters indicated by fill color.
873 (**F**) UMAP plots of glutamatergic markers *SLC17A6* (*VGLUT2*) and *SLC17A7* (*VGLUT1*). Color
874 indicates normalized transcript level.
875 (**G**) VoxHunt correlation analysis mapping clusters ExN1-4 onto the E15 mouse brain.
876 (**H**) VoxHunt correlation analysis mapping the PT/ZLI/rTh cluster onto the E15 mouse brain.
877 (**I**) UMAP plots of the PT/ZLI/rTh cluster, demonstrating the expression of markers associated
878 with the PT, ZLI, and rTh. Transcript information is indicated by color. The relative locations of
879 these structures within the developing diencephalon are shown in the schematic.
880 (**J**) Example traces showing voltage and AP responses to current injections in cells recorded
881 from an hThO.
882 (**K**) Pseudotime ordering of cells within the hThOs.
883 (**L**) UMAP plot of the neural progenitor marker *TNC*. Color indicates the normalized transcript
884 level.
885 (**M-N**) UMAP plots of cell cycle analysis results for the Cycling Progenitor, Radial Glia, and Glia
886 cell clusters. Color indicates S Score (**M**) or G2M Score (**N**).
887 (**O**) UMAP plot of the astrocyte marker *GFAP* in the Cycling Progenitor, Radial Glia, and Glia
888 cell clusters. Color indicates the normalized transcript level.
889 Data in (**C-I**) and (**K-O**) were produced by snRNA-seq analysis of 15,363 nuclei from D90
890 hThOs.
891 See also **Figures S1-S3** for additional data validating hiPSC lines and hThOs. See **Figure S4**
892 for additional data related to electrophysiological properties and synapses in hThOs.
893
894

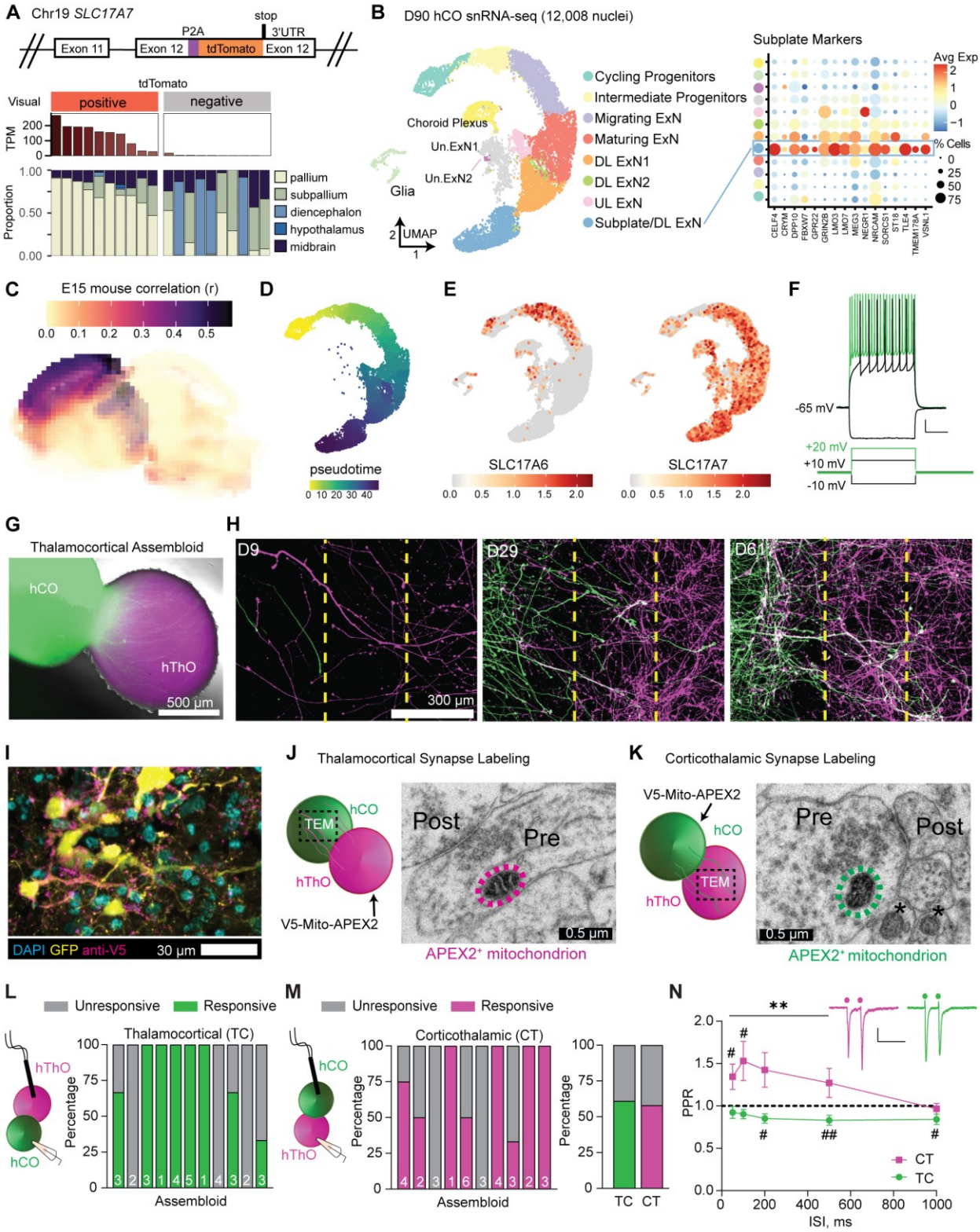

Figure 2. Fusing hThOs and hCOs produces assembloids with functional synapses. (**A**) Reporter line validation for hCOs. Top: Schematic of *SLC17A7* (*VGLUT1*) exon 12 in the TP-190a-VGLUT1-tdTomato reporter line, which was used to generate all hCOs. Bottom: VoxHunt deconvolution analysis of bulk RNA-seq data from D70 hCOs using E13 mouse brain data from the *Allen Brain Atlas* as a reference. Organoids were visually categorized as positive

901 or negative for tdTomato fluorescence prior to sequencing. The *tdTomato* RNA level for each
902 sample is indicated in TPM (transcripts per million). Each stacked bar indicates one bulk RNA-
903 seq sample derived from 2-3 pooled organoids.
904 (**B**) The snRNA-seq analysis of hCOs. Left: UMAP plot with cluster annotations. ExN: excitatory
905 neuron, DL: deep layer, UL: upper layer, Un.: unknown. Right: Dot plot showing subplate marker
906 expression by cluster. Avg Exp: normalized average expression, % Cells: percentage of cells
907 expressing a marker within a cluster.
908 (**C**) VoxHunt analysis mapping hCOs (all clusters) onto the E15 mouse brain.
909 (**D**) Pseudotime analysis of the neural cell trajectory (Cycling Progenitors to UL ExNs, DL ExNs,
910 and Subplate/DL ExNs) from hCOs.
911 (**E**) UMAP plots of glutamatergic markers *SLC17A6* (*VGLUT2*) and *SLC17A7* (*VGLUT1*). Color
912 indicates normalized transcript level.
913 (**F**) Traces showing the voltage and AP responses in cells recorded from an hCO.
914 (**G**) Fluorescence and bright field image of a TC assembloid at 5 days postfusion (dpf).
915 (**H**) Representative fluorescence images for 2-dimensional fusion assay. Thalamic neurons
916 (magenta, right chamber) and cortical neurons (green, left chamber) extend processes from
917 their respective chambers, across the barrier region (dashed yellow lines), and into the opposite
918 chamber starting at D9. Elaborate processes extending from the opposite sides can be seen in
919 both halves by D61.
920 (**I**) Fluorescence image of an hCO co-transduced with hSyn-GFP and hSyn-V5-Mito-APEX2
921 lentiviruses.
922 (**J**) Schematic and TEM image of an APEX2^{+} mitochondrion (circled in magenta) in a TC
923 synapse. Pre: presynaptic compartment, post: postsynaptic compartment.
924 (**K**) Schematic and TEM image of an APEX2^{+} mitochondrion (circled in green) in a CT synapse.
925 APEX2^{-} mitochondria are indicated by asterisks (*).
926 (**L**) Left: Schematic of the recording configuration for the TC pathway. Right: Bar graph of the
927 percentage of responsive (green) and unresponsive (gray) cells in 11 assembloids. The
928 numbers of cells recorded per assembloid are shown in the bars.
929 (**M**) Left: Schematic of the recording configuration for the CT pathway. Middle: The percentages
930 of hThO cells that responded (magenta) or did not respond (gray) to hCO stimulation across 10
931 assembloids. Right: Bar graph of the average percentage of responsive cells for TC and CT
932 synapses, based on (**G**) and (**H**).
933 (**N**) Line graph of PPRs across five interstimulus intervals (ISIs) in CT (magenta) and TC (green)
934 synapses [one-sample *t*-test: $\mu = 1$, #p <0.05, ##p <0.01, n = 18-23 cells/9-13 assembloids
935 (TC), n = 8-24/7-12 (CT)]. Differences between CT and TC synapses were evaluated by
936 unpaired *t*-test (**p <0.01). Inset: Sample traces depicting PPRs in CT and TC synapses.
937 Circles represent stimulus artifacts.
938 Grouped data are shown as mean ± SEM. Scale bars (**F**): 10 mV, 2.5 s. Scale bars (**N**): 20 pA,
939 200 ms.
940 See also **Figures S1 and S5** for additional data validating the TP-190a-VGLUT1-tdTomato
941 reporter line and hCOs, respectively. See **Figure S4** for additional data related to
942 electrophysiological properties and synapses in hCOs.
943
944

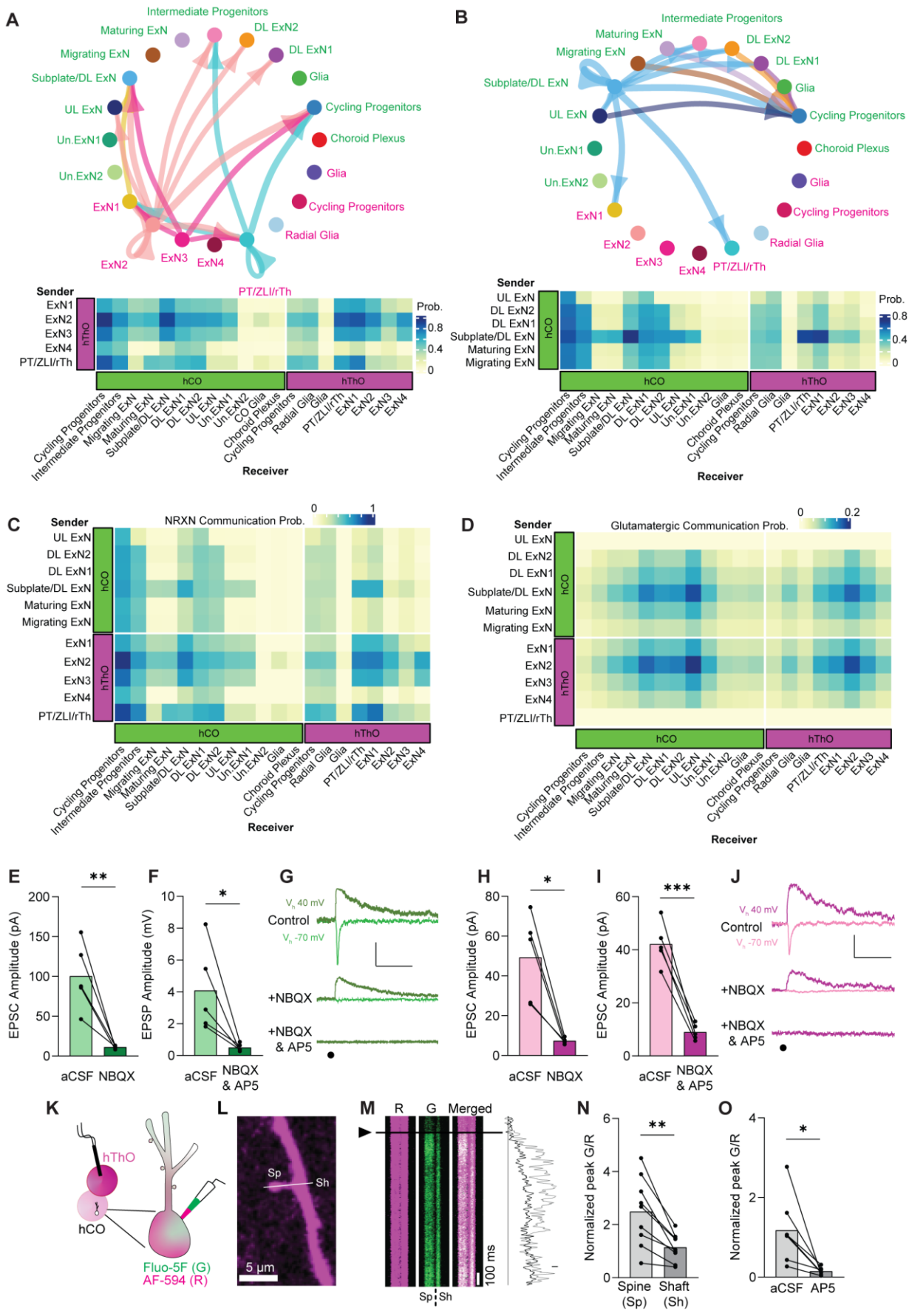
A
Intermediate Progenitors
Maturing ExN
DL ExN2
Migrating ExN
DL ExN1
Subplate/DL ExN
Glia
UL ExN
Cycling Progenitors
Un.ExN1
Choroid Plexus
Un.ExN2
Glia
ExN1
Cycling Progenitors
Radial Glia
ExN2
ExN3
ExN4
B
Intermediate Progenitors
Maturing ExN
DL ExN2
Migrating ExN
DL ExN1
Subplate/DL ExN
Glia
UL ExN
Cycling Progenitors
Un.ExN1
Choroid Plexus
Un.ExN2
Glia
ExN1
Cycling Progenitors
Radial Glia
ExN2
ExN3
ExN4
PT/ZLI/rTh
Sender
Receiver
hCO
hThO
Prob.
C
NRXN Communication Prob.
D
Glutamatergic Communication Prob.
E
EPSC Amplitude (pA)
aCSF
NBQX
F
EPSP Amplitude (mV)
aCSF
NBQX & AP5
G
Control
+NBQX
+NBQX & AP5
H
EPSC Amplitude (pA)
aCSF
NBQX
I
EPSC Amplitude (pA)
aCSF
NBQX & AP5
J
Control
+NBQX
+NBQX & AP5
K
hThO
hCO
Fluo-5F (G)
AF-594 (R)
L
Sp
Sh
5 µm
M
R
G
Merged
100 ms
Sp
Sh
N
Normalized peak G/R
Spine (Sp)
Shaft (Sh)
O
Normalized peak G/R
aCSF
AP5

946 **Figure 3. Assembloids contain glutamatergic TC and CT synapses.**
947 (**A**) NeuronChat predictions showing communication between cell clusters containing
948 glutamatergic neurons in hThOs and other cell clusters in hCOs and hThOs. Probability of
949 communication (Prob) is indicated in the heatmap (bottom). Interactions with a Prob >0.6 are
950 shown in the circle plot (top).
951 (**B**) NeuronChat predictions showing communication between cell clusters containing
952 glutamatergic neurons in hCOs and other cell clusters in hCOs and hThOs. Probability is
953 indicated in the heatmap (bottom). Interactions with a Prob >0.5 are shown in the circle plot
954 (top).
955 (**C**) Heatmap showing the probability of NRXN-mediated communication between cell clusters in
956 hCOs and hThOs. Predictions were made using NeuronChat.
957 (**D**) Heatmap showing the probability of glutamatergic communication between cell clusters in
958 hCOs and hThOs. Predictions were made using NeuronChat.
959 (**E**) Average TC EPSC amplitude [holding potential (Vh) –70 mV] in the presence of NBQX (3
960 mM) is significantly decreased compared to control aCSF conditions (paired *t*-test: **p = 0.009,
961 n = 5 cells/2 assembloids).
962 (**F**) The average TC EPSP amplitude (Vh +40 mV) in the presence of NBQX and AP5 (50 μM) is
963 significantly lower than in control aCSF (paired *t*-test: *p = 0.038, n = 5 cells/3 assembloids).
964 (**G**) Traces of evoked TC AMPAR- and NMDAR-mediated currents in control aCSF and in the
965 presence of NBQX or NBQX and AP5, respectively. Circle represents a stimulus artifact.
966 (**H**) Average CT EPSC amplitude (Vh –70 mV) in the presence of NBQX is significantly
967 decreased compared to control aCSF conditions (paired *t*-test: *p = 0.012, n = 5 cells/3
968 assembloids).
969 (**I**) The average CT EPSC amplitudes (Vh +40 mV) are significantly reduced in the presence of
970 NBQX and AP5 compared to control aCSF (paired *t*-test: ***p = 0.0006, n = 5 cells/3
971 assembloids).
972 (**J**) Example traces of evoked CT AMPAR- and NMDAR-mediated currents in aCSF and in the
973 presence of NBQX or NBQX and AP5, respectively.
974 (**K**) Schematics of two-photon calcium imaging in postsynaptic dendritic spines of hCO cells
975 upon hThO stimulation. Alexa Fluor 594: AF-594 (R), magenta; Fluo-5F (G), green.
976 (**L**) Image of a dendrite of an hCO cell. Line scans (white line) were performed across a
977 dendritic spine (Sp) and parent dendritic shaft (Sh).
978 (**M**) Left: Representative changes in G/R of Sp and Sh responses over time to a single synaptic
979 stimulation (arrowhead and black line). Right: Representative line scans of Sp (light gray) and
980 Sh (dark gray).
981 (**N**) Average changes in synaptically evoked G/R (paired *t*-test: **p = 0.002, n = 9 cells/4
982 assembloids).
983 (**O**) Average changes in synaptically evoked Sp G/R in aCSF and in the presence of AP5
984 (paired *t*-test: *p = 0.018, n = 7 cells/5 assembloids).
985 Data in (**E**), (**F**), (**H**), (**I**), (**N**), and (**O**) are shown as the average values with individual responses
986 overlaid. Scale bars (**G**), (**J**): 40 pA, 100 ms. Scale bar (**M**): 20% G/R.
987 See also **Figure S6** for snRNA-seq data supporting the NeuronChat predictions in (**A**) to (**D**).
988
989

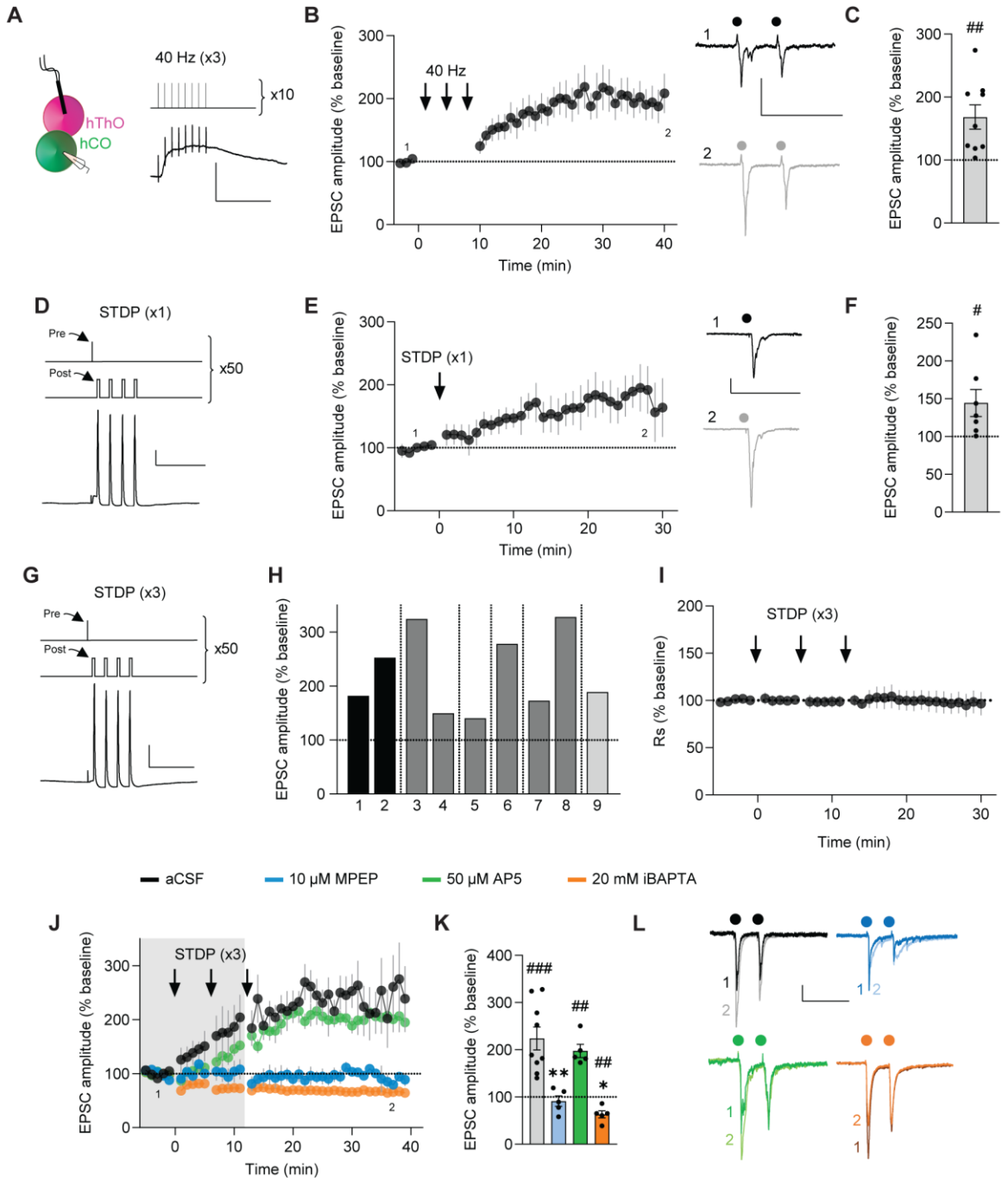

990
991 **Figure 4. TC synapses in assembloids undergo LTP via multiple protocols.**
992 (**A**) Left: Schematic of the recording configuration. Right, top: 40-Hz electrical stimulation LTP-
993 induction protocol. Right, bottom: Representative trace of a response to 10-Hz stimulation.
994 (**B**) Left: Time course data demonstrating that 40-Hz stimulation repeated three times (arrows)
995 induces LTP in TC assembloids (n = 9 cells/9 assembloids). Right: Representative traces from
996 the first 5 min (1, dark) and final 5 min (2, light) of the experiment. Circles indicate electrical
997 stimuli.
998 (**C**) Bar graph of group data after 40-Hz induction from (**B**) shows EPSC amplitudes significantly
999 differ from baseline values (one-sample *t*-test, μ = 100, ##p = 0.0077).

(**D**) Top: Spike-timing–dependent plasticity (STDP) was induced by stimulating presynaptic hThO inputs (Pre) and then delivering four current injections (2-nA) to the postsynaptic cell (Post), repeated 50 times. Bottom: Representative trace of an hCO cell's response to stimulation and depolarization.
(**E**) Left: Time course data demonstrating that the short (×1) STDP protocol (arrow) in TC assembloids induces LTP (n = 7 cells /3 assembloids). Right: Representative traces from the first (dark) and final (light) 5 min of the experiment.
(**F**) Bar graph of group data following the ×1 STDP induction from (**E**) shows that EPSC amplitudes significantly differ from baseline values (one-sample *t*-test, μ = 100, #p = 0.04).
(**G**) Top: Long (×3) STDP-induction protocol, as in (**D**) but repeated three times every 5 min. Bottom: Representative trace of a response to stimulation and depolarization.
(**H**) Bar graph showing the average responses from nine cells from six assembloids after TC LTP induction. Shades of gray indicate different batches of assembloids; vertical lines denote separate assembloids.
(**I**) Time course of series resistance (Rs) normalized to the 5-min baseline period demonstrating TC LTP is not due to changes in Rs.
(**J**) Time course demonstrating the ×3 STDP protocol (arrows) induces LTP in TC synapses (black, n = 9 cells/6 assembloids). MPEP (blue, n = 5 cells/4 assembloids) or iBAPTA blocked LTP (orange, n = 5 cells/3 assembloids). AP5 did not block TC LTP (green, n = 5 cells/2 assembloids). Shaded area depicts the presence of bath-applied drugs.
(**K**) Bar graph of group data following ×3 STDP induction from (**J**). Differences from baseline were evaluated by one-sample *t*-test (μ = 100, ##p <0.01, ###p <0.0001). Differences between treatments and aCSF were evaluated by one-way ANOVA, p <0.0001. Dunnett's test: *p <0.05, *p <0.01.
(**L**) Example traces from the first (1) and final (2) 5 min of the experiment across conditions. Scale bars for (**A**): 20 mV, 200 ms. Scale bars for (**B**), (**E**): 50 pA, 200 ms. Scale bars for (**D**), (**G**): 40 mV, 100 ms. Scale bars for (**L**): 20 pA, 200 ms. Data shown are mean ± SEM (**B**), (**E**), (**I**), and (**J**), with individual data points overlaid as dots in (**C**), (**F**), and (**K**).
For (**B**), (**E**), (**J**), and (**L**) the first (1) and final (2) 5 min of the experiment are noted.
See also **Figure S7** for analysis of paired-pulse ratio (PPR) measures.

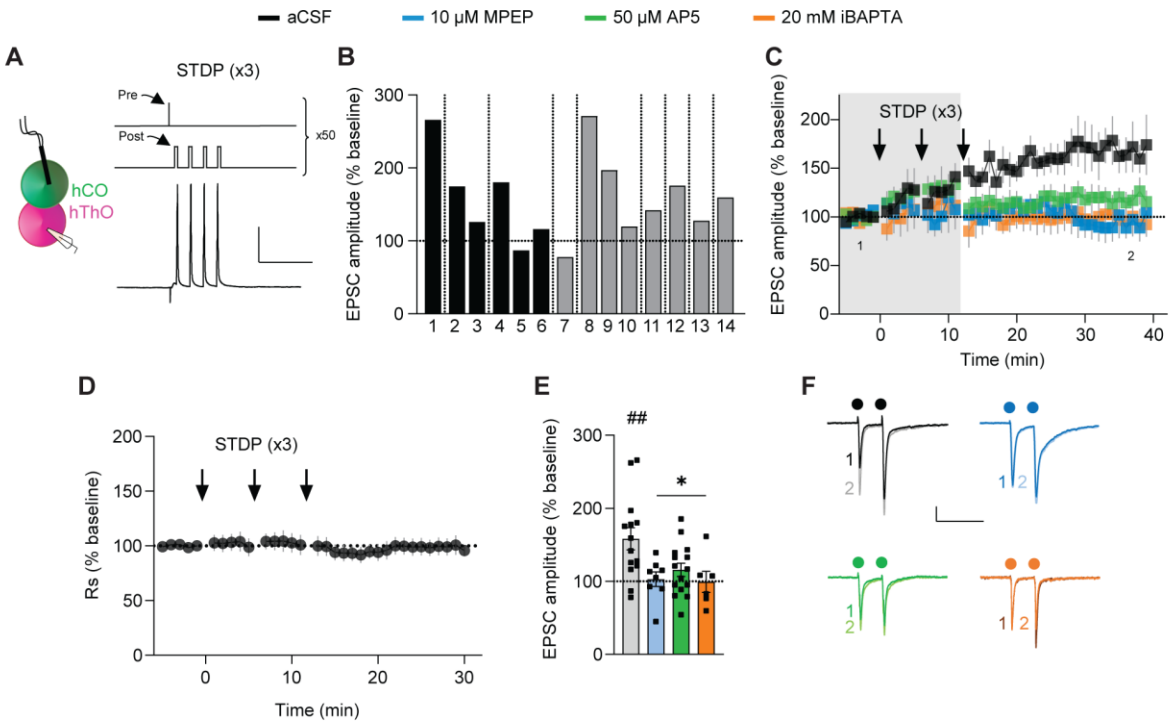

Figure 5. CT synapses in assembloids undergo LTP.

(**A**) Left: Schematic of the recording configuration to induce CT LTP. Right: The long (×3) STDP-induction protocol and example response.

(**B**) Bar graph showing the average responses in 14 cells from 9 assembloids after CT LTP induction in aCSF. Shades of gray indicate different batches of assembloids; vertical lines denote separate assembloids.

(**C**) Time course demonstrating that ×3 STDP delivery (arrows) induces LTP in CT synapses (black, n = 14 cells/9 assembloids). MPEP (blue, n = 8 cells/6 assembloids), AP5 (green, n = 15 cells/7 assembloids), or iBAPTA (orange, n = 6 cells/2 assembloids) blocked LTP. Shaded area depicts the presence of bath-applied drugs. The first (1) and final (2) 5 min of the experiment are noted.

(**D**) Time course of Rs demonstrating that CT LTP is not due to changes in Rs.

(**E**) Bar graph of group data from (**C**). Differences from baseline were evaluated by one-sample t-test (μ = 100, ##p <0.01). Differences between treatments and aCSF were evaluated by one-way ANOVA, p = 0.0083. Dunnett's test: *p <0.05.

(**F**) Example traces from the first (1) and final (2) 5 min of the experiment across conditions. Circles indicate electrical stimulation.

Scale bars for (**A**): 40 mV, 100 ms. Scale bars for (**F**): 50 pA, 200 ms. Data shown are mean ± SEM (**C**), (**D**) with individual data points overlaid in (**E**).

See also **Figure S7** for PPR analysis.

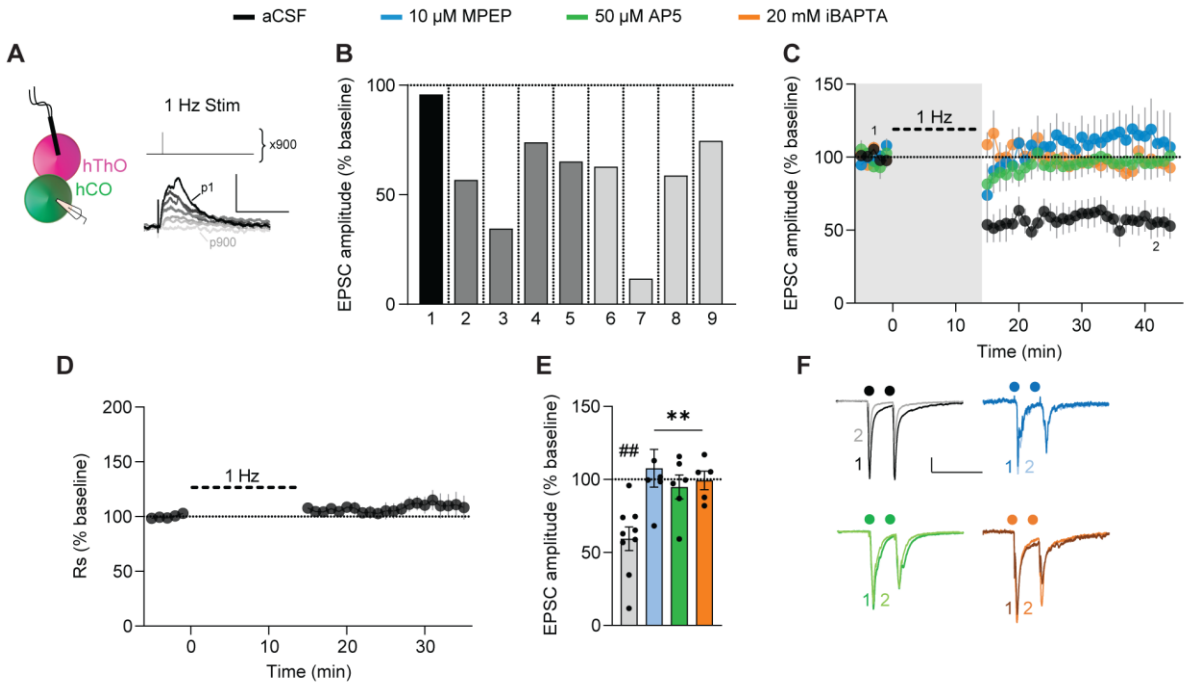

Figure 6. TC synapses in assembloids undergo LTD.

(**A**) Left: Schematic of the recording configuration to induce TC LTD. Right, top: LTD was induced with electrical stimulation delivered at 1 Hz for 900 pulses. Bottom: Example responses of a cell to a subset of the 900 pulses, dark-to-light traces depict the responses as the number of pulses progressed (from pulse (p) 1 to p900).

(**B**) Bar graph showing the average responses from nine individual cells from nine assembloids after TC LTD induction in aCSF. Shades of gray indicate different batches of assembloids; vertical lines denote separate assembloids.

(**C**) Time course data demonstrating that 1-Hz electrical stimulation (thick dashed line) induces LTD in TC synapses (black, n = 9 cells/9 assembloids). MPEP (blue, n = 6 cells/4 assembloids), AP5 (green, n = 6 cells/5 assembloids), or iBAPTA (orange, n = 5 cells/4 assembloids) blocked LTD. Shaded area depicts the presence of bath-applied drugs. The first (1) and final (2) 5 min of the experiment are noted.

(**D**) Time course of Rs normalized to the 5-min baseline period, demonstrating that TC LTD is not due to changes in Rs.

(**E**) Bar graph of group data after 1-Hz stimulation from (**C**). Differences from baseline were evaluated by one-sample *t*-test (μ = 100, ##p <0.01). Differences between treatments and aCSF were evaluated by one-way ANOVA, p = 0.0034. Dunnett's test: **p <0.01.

(**F**) Example traces from the first (1) and final (2) 5 min of the experiment across conditions. Circles indicate electrical stimulation.

Scale bars for (**A**): 5 mV, 100 ms. Scale bars for (**F**): 40 pA, 200 ms. Data shown are mean ± SEM (**C**), (**D**), and (**E**), with individual data points overlaid in (**E**).

See also **Figure S7** for PPR analysis.

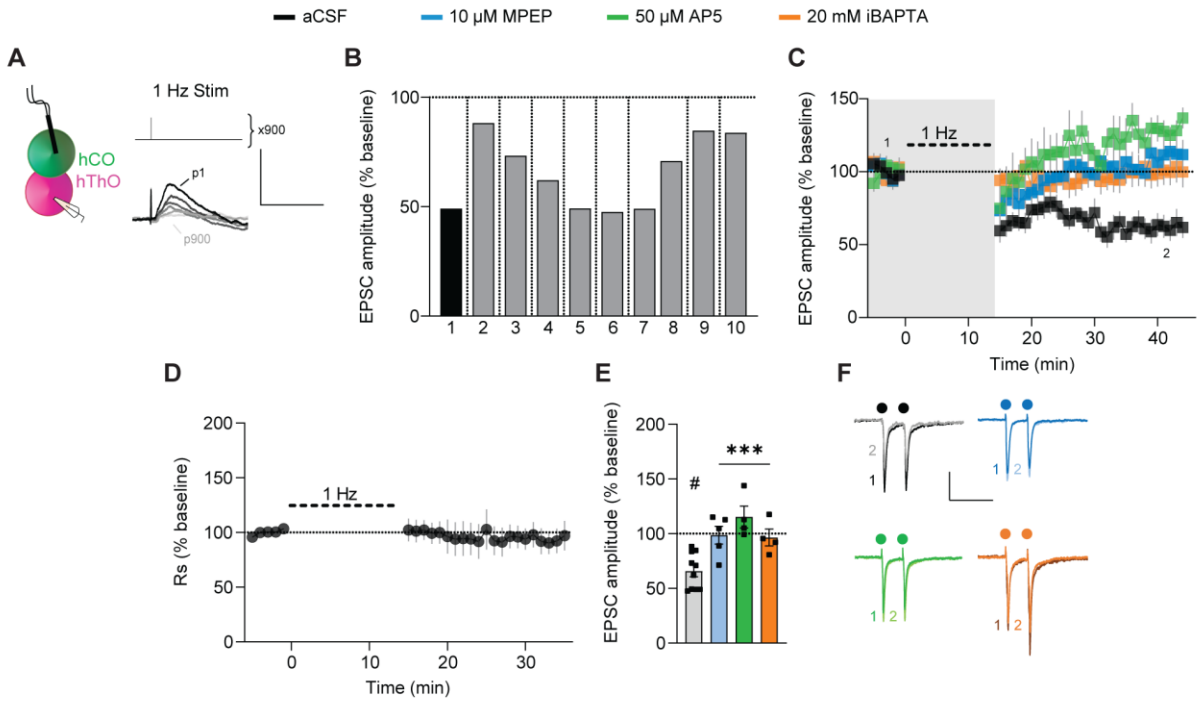

Figure 7. CT synapses in assembloids undergo LTD.

(**A**) Schematic of the experimental condition for CT LTD induction and the 1-Hz LTD-induction protocol.

(**B**) Bar graph of the average responses of 10 individual cells from 9 assembloids after CT LTD induction in aCSF. Shades of gray indicate different batches of assembloids; vertical lines denote separate assembloids.

(**C**) Time course data show that 1-Hz stimulation (thick dashed line) induced LTD in CT synapses (black, n = 10 cells/9 assembloids). MPEP (blue, n = 5 cells/5 assembloids), AP5 (green, n = 4 cells/3 assembloids), or iBAPTA (orange, n = 4 cells/4 assembloids) blocked LTD induction. Shaded area depicts the presence of bath-applied drugs. The first (1) and final (2) 5 min of the experiment are noted.

(**D**) Time course of Rs normalized to the 5-min baseline period, demonstrating that CT LTD is not due to changes in Rs.

(**E**) Bar graph of group data after 1-Hz stimulation from (**C**). Differences from baseline were evaluated by one-sample *t*-test (μ = 100, #p <0.05). Differences between treatments and aCSF were evaluated by one-way ANOVA, p = 0.0004. Dunnett's test: ***p <0.001.

(**F**) Example traces from the first (1) and final (2) 5 min of the experiment across conditions. Circles indicate electrical stimulation.

Scale bars for (**A**): 5 mV, 100 ms. Scale bars for (**F**): 50 pA, 200 ms. Data shown are mean ± SEM (**C**), (**D**), and (**E**), with individual data points overlaid in (**E**).

See also **Figure S7** for PPR analysis.

1105 **STAR Methods**

1106 **Human iPSC culture**

1107 The use of hiPSCs for the generation of organoids was approved by the St. Jude Institutional
1108 Review Board. TP-190a and TP-189 were derived from dental pulp cells from neurotypical male
1109 and female subjects, respectively, with normal karyotypes. Cells were reprogrammed using
1110 episomal plasmids (ALSTEM LLC). The 2242 (i.e., 2242-1), 1205 (i.e., 1205-4), and 8858 (i.e.,
1111 8858-3) lines/clones were previously published.[95]

1112 All hiPSC lines were maintained in culture on human ES-qualified Matrigel (5264004,
1113 Corning) in complete mTeSR Plus (100-0276, STEMCELL Technologies) at 5% O_2, 37 °C, and
1114 5% CO_2. The cultures were passaged with Versene (15040066, ThermoFisher). Genetically
1115 modified reporter hiPSC lines were validated before differentiation (**Figure S1**). Specifically, six
1116 assays were performed: (1) Colonies were immunostained for six pluripotency markers[96]
1117 (Stemlight Pluripotency Antibody Kit 9656S, Cell Signaling); (2) Expression of five additional
1118 pluripotency markers[96] was assayed using a Custom TaqMan RT-qPCR assay designed in-house
1119 (manufactured by ThermoFisher); (3) G-banding; (4) Copy number variation at the seven most
1120 frequently aberrant chromosomal locations[97–99] was assayed using a custom TaqMan RT-qPCR
1121 assay designed in-house (manufactured by ThermoFisher); (5) Global methylation analysis
1122 (Infinium MethylationEPICv1.0 850K Beadchip) was performed to identify methylation status at
1123 select epigenetic markers,[100,101] and results were then compared to established and previously
1124 published hiPSC lines;[102]; (6) Trilineage assay (STEMdiff Trilineage Differentiation Kit 05230,
1125 STEMCELL Technologies) was performed, and markers of interest[96] were analyzed using a
1126 Custom TaqMan RT-qPCR assay designed in-house (manufactured by ThermoFisher).

1127

1128 **Generating reporter lines**

1129 Genome-edited TP-190a hiPSCs were generated using CRISPR-Cas9 technology. Briefly,
1130 hiPSCs were pretreated with StemFlex (Thermo-Fisher Scientific) supplemented with 1×

1131 RevitaCell (ThermoFisher Scientific) for 1 h. Then, approximately 10^6 cells were transiently
1132 transfected with precomplexed ribonuclear proteins consisting of 250 pmol chemically modified
1133 single-guide RNA (sgRNA; Synthego), 165 pmol Cas9 protein (St. Jude Protein Production Core),
1134 500 ng pMaxGFP (Lonza), and 3 µg ssODN donor (for deletion) or 1 µg dsDNA donor (for tagging)
1135 via nucleofection (Lonza, 4D-Nucleofector™ X-unit) using solution P3 and program CA-137 in a
1136 large (100-µL) cuvette, according to the manufacturer's recommended protocol. Five days
1137 postnucleofection, cells were single-cell sorted by FACS for GFP^+ (transfected) cells and plated
1138 onto Vitronectin XF (Stem Cell Technologies)-coated plates into prewarmed (37°C) StemFlex
1139 media supplemented with 1× CloneR (Stem Cell Technologies).

1140 Clones were screened for the desired modification via targeted deep sequencing using
1141 gene-specific primers with partial Illumina adapter overhangs on a Miseq Illumina sequencer, as
1142 previously described,[103] or by junction PCR followed by sequencing. Briefly, cell pellets of
1143 approximately 10,000 cells were lysed and used to generate gene-specific amplicons with partial
1144 Illumina adapters in PCR#1. Amplicons were indexed in PCR#2 and pooled with targeted
1145 amplicons from other loci to create sequence diversity. Additionally, 10% PhiX Sequencing
1146 Control V3 (Illumina) was added to the pooled amplicon library prior to running the sample on a
1147 Miseq Sequencer System (Illumina) to generate paired 2 × 250-bp reads. Samples were de-
1148 multiplexed using the index sequences, fastq files were generated, and next-generation
1149 sequencing (NGS) analysis of clones was performed using CRIS.py.[104] Correctly edited clones
1150 were identified, expanded, and sequence confirmed. Final clones were authenticated using the
1151 PowerPlex® Fusion System (Promega), which was performed at the St. Jude Hartwell Center
1152 and tested for mycoplasma by using the MycoAlertTMPlus Mycoplasma Detection Kit (Lonza).
1153 Editing-construct sequences and relevant primers are listed in **Table S1**.
1154

1155 **Thalamic organoid generation**

1156 The hThOs were generated from TCF7L2-tdTomato reporter hiPSC lines, except for indicated
1157 organoids in **Figure S2**. For differentiation, cryovials were plated and maintained in culture in
1158 mTeSR1 (85850, STEMCELL Technologies). At 80% confluency, they were dissociated into
1159 single cells with Accutase (AT-104, Innovative Cell Technologies) and plated into low-attachment
1160 96-well V-bottom plates (MS-9096VZ, Sbio) at 10,000 cells/well, in gfCDM media (1:1 IMDM
1161 (12440053, Thermofisher): Ham's F12 (12-615F, Lonza), 1× lipid concentrate (11905031,
1162 Thermofisher), 1× antibiotic-antimycotic (15240062, Gibco), 450 μM monothioglycerol (M6145,
1163 Sigma), 15 μG/mL apotransferrin (T1428, Sigma), 5 mg/mL BSA (50-255-465, Fisher Scientific)
1164 supplemented with 5 μM SB-431542 (TGFβ inhibitor, 1614, Tocris), 1 μg/mL insulin (I9278,
1165 Sigma), 1% v/v growth factor–reduced (GFR) Matrigel (354230, Corning), 2 μM thiazovivin
1166 (72254, STEMCELL Technologies). On Day (D) 2, half the media was replaced with the same
1167 media supplemented with 4 μM dorsomorphin (3093, Tocris). On D4 and D6, half of the media
1168 was replaced with gfCDM supplemented with 5 μM SB-431542, 100 nM Smoothened agonist
1169 (73414, STEMCELL Technologies), and 20 ng/mL Fgf8b (100-25, PeproTech). In some
1170 differentiations, Matrigel was added on D2 instead of D0, but no difference was detected in the
1171 resulting organoids. On D8, D10, and D12, three-fourths of the media was replaced with the same
1172 but further supplemented with 30 ng/mL BMP7 (354BP010, R&D Systems) and 1 μM MEKi
1173 PD0325901 (S1036, R&D Systems). On D14, D16, and D18 half the media was replaced with the
1174 same, but gfCDM was substituted with thalamic N2 media (DMEM:F12, 10% ES-FBS (ES-009-
1175 C, SIGMA), 1× N2 supplement (17502-048, Gibco), 1× Glutamax (35050061, Gibco), and 1×
1176 antibiotic-antimycotic.

1177 On D20, all organoids were transferred to a magnetic stir bioreactor (BWS-S03N0S-6,
1178 ABLE Corporation, Tokyo) in thalamic N2 media and agitated at 40 rpm. On D22 and D24, half
1179 the media was replaced with thalamic N2 supplemented with 1× B27 without vitamin A (12587-
1180 010, Gibco), 20 ng/mL heat-stable bFGF (PHG0367, ThermoFisher) and 20 ng/mL EGF (AF-100-

1181 15-100UG, Peprotech). On D26 and D28, half the media was replaced with the same, but the
1182 concentrations of bFGF and EGF were reduced to 10 ng/mL. On D30 and D32, all the media was
1183 replaced with thalamic N2 supplemented with 1× B27 without vitamin A.

1184 Starting D35, full media was replaced every 4 days with BrainPhys (05790, STEMCELL
1185 Technologies) supplemented with 1× N2, 1× B27 without vitamin A, 10% ES-FBS, 10 ng/mL
1186 BDNF (450-02, Peprotech), and 10 ng/mL GDNF (450-10, Peprotech). Starting D70, all the media
1187 was changed to BrainPhys supplemented with 1× N2, 1× B27 without vitamin A, 1× glutamax, 1×
1188 NEAA (11140050, Gibco), 1× antibiotic-antimycotic, 200 μM ascorbic acid (A4403, Sigma), 100
1189 μM dibutyryl cAMP (D0627, Sigma), 1% ES-FBS, 10 μM DAPT (2634, Tocris), 20 ng/mL BDNF,
1190 and 20 ng/mL GDNF. Starting D82, the concentration of BDNF and GDNF was reduced to 10
1191 ng/mL. In addition, after D30, large organoids were pinched into two halves by using a pair of
1192 ultra-fine clipper scissors (15300-00, Fine Science Tools) every 5–7 days to avoid large necrotic
1193 centers.

1194

1195 **Cortical organoid generation**

1196 The hCOs were generated from VGLUT1-tdTomato reporter iPSC lines. At 80% confluency, cell
1197 cultures were dissociated into single cells with Accutase (AT-104, Innovative Cell Technologies),
1198 and plated into low-attachment 96-well V-bottom plates (MS-9096VZ, Sbio) at 9000 cells/well, in
1199 EB media (DMEM:F12, 20% knockout serum replacement (KSR) (10828, Life Technologies), 3%
1200 ES-FBS, 1× Glutamax, 1× β-mercaptoethanol (2020-07-30, Gibco), 1× antibiotic-antimycotic)
1201 supplemented with 5 μM SB-431542 (TGFβ inhibitor, 1614, Tocris), 2 μM dorsomorphin (3093,
1202 Tocris), 3 μM IWR1e (Wnt inhibitor, 681669, EMD Millipore), 1% v/v GFR-Matrigel, and 2 μM
1203 thiazovivin.

1204 In some differentiations, 0% or 0.5% v/v GFR-Matrigel was added on D0 but no difference
1205 in the resulting organoids was detected. On D2, half the media was replaced with the same but
1206 without Matrigel. On D4 and D6, half the media was replaced with GMEM KSR media (GMEM,

1207 20% KSR, 1× NEAA (Gibco), 1× sodium pyruvate (11360070, Gibco), 1× β-mercaptoethanol, 1×
1208 antibiotic-antimycotic) supplemented with 5 μM SB-431542, 3 μM IWR1e, 2.5 μM cyclopamine
1209 (72074, STEMCELL Technologies), and 2 μM thiazovivin. On D8, half the media was replaced
1210 with GMEM KSR media supplemented with 5 μM SB-431542, 3 μM IWR1e, and 2.5 μM
1211 cyclopamine. On D10, D12, D14, and D16, half the media was replaced with GMEM KSR media
1212 supplemented with 5 μM SB-431542 and 3 μM IWR1e. On D18 and D20, half the media was
1213 replaced with CBO N2 media (DMEM:F12, 1× chemically defined lipid concentrate (11905-031,
1214 Life Technologies), 1× N2 supplement (17502-048, Gibco) and 1× antibiotic-antimycotic)
1215 supplemented with 1× B27 supplement without vitamin A (12587-010, Gibco), 20 ng/mL heat-
1216 stable bFGF, and 20 ng/mL EGF. On D22, organoids were transferred to a magnetic stir
1217 bioreactor (BWS-S03N0S-6, ABLE Corporation) in CBO N2 media supplemented with 1× B27
1218 supplement without vitamin A, 20 ng/mL heat-stable bFGF and 20 ng/mL EGF, and agitated at
1219 40 rpm. Half of the media was replaced with the same on D24, D26, and D28. On D30, the media
1220 was changed to CBO FBS media (DMEM:F12, 1× chemically defined lipid concentrate (11905-
1221 031, Life Technologies), 1× N2 supplement, 10% ES-FBS, 5 μg/mL heparin and 1× antibiotic-
1222 antimycotic) supplemented with 1× B27 supplement without vitamin A. Full media was replaced
1223 every 4 days. On D42 and D46, the media was changed to CBO FBS media supplemented with
1224 1× B27 supplement without vitamin A, 10 ng/mL BDNF (450-02, Peprotech), and 10 ng/mL GDNF
1225 (450-10, Peprotech). Starting D50, all the media was replaced every 4 days with BrainPhys
1226 (05790, STEMCELL Technologies) supplemented with 1× N2 supplement, 50× B27 supplement
1227 without vitamin A, 10% ES-FBS, 10 ng/mL BDNF and 10 ng/mL GDNF. Starting D70, media was
1228 changed to BrainPhys supplemented with 1× N2, 50× B27 without vitamin A, 1× glutamax, 1×
1229 NEAA, 1× antibiotic-antimycotic, 200 μM ascorbic acid, 100 μM cAMP, 1% ES-FBS, 10 μM DAPT,
1230 20 ng/mL BDNF, and 20 ng/mL GDNF. Starting at D82, the concentration of BDNF and GDNF
1231 was reduced to 10 ng/mL. In addition, after D30, large organoids were pinched into 2 halves by
1232 using a pair of ultra-fine clipper scissors every 5–7 days to avoid large necrotic centers.

1233

1234 **Generation of thalamocortical assembloids**

1235 Between D90 and D120, TCF7L2-tdTomato$^+$ hThOs were paired with VGLUT1-tdTomato$^+$ hCOs
1236 of similar age. Each pair was transferred to a well of a low-attachment, 24-well plate in 500 mL
1237 Fusion media (BrainPhys supplemented with 1× N2, 50× B27 without vitamin A, 1× glutamax, 1×
1238 NEAA, 1× antibiotic-antimycotic, 200 μM ascorbic acid, 100 μM cAMP, 1% ES-FBS, 10 μM DAPT,
1239 20 ng/mL BDNF, 20 ng/mL GDNF, and the CEPT cocktail (50 nM Chroman 1 [HY-15392,
1240 MedChem Express], 5 μM emricasan (S7775, Selleckchem), 0.7 μM trans-ISRIB (#5284, Tocris),
1241 and polyamine supplement (#P8483, Sigma-Aldrich[105]) supplemented with 0.5% v/v GFR-
1242 Matrigel. The plate was left tilted and undisturbed in the incubator. After 3 days, 60% of the media
1243 in each well was replaced with fusion media. This was done slowly, while keeping the plate tilted
1244 with minimal disturbance to the "fused" organoid pair in each well. The same was done on D6 and
1245 D9. Subsequently, 80% of the media was replaced every 3 days. On D4, the plate was transferred
1246 to an orbital shaker at 80 rpm. The shaker speed was increased to 90 rpm on D5, 100 rpm on D6,
1247 and starting D7, the assembloids were kept at 110 rpm. Between 5 and 10 weeks postfusion,
1248 assembloids were harvested for electrophysiological experiments.

1249

1250 **Plasmids and lentiviruses**

1251 Synapsin-EGFP (hSyn-GFP) lentiviruses with the VSV-G pseudo-type were generated using the
1252 pHR-hSyn-eGFP plasmid[106] (Addgene: 114215, a gift from Xue Han) by the St. Jude Viral Vector
1253 Core. For APEX2 experiments, pLenti-hSyn-V5-COX4-APEX2 plasmid was generated by cloning
1254 the V5-COX4-APEX2 sequence from pAAV-COX4-dAPEX2[54] (Addgene: 117176, a gift from
1255 David Genty) into the pLenti backbone containing the human *SYN* promoter. Briefly, pAAV-COX4-
1256 APEX2 was digested with BspE1 and EcoR1, and pLenti-hSyn-nucGFP[107] (Addgene: 140190, a
1257 gift from Lorenz Studer) was digested with EcoRI and AgeI to remove the nucGFP-coding
1258 sequence. Insert containing the V5-COX4-APEX2 sequence was then ligated into the pLenti-hSyn

1259 backbone. The resulting plasmid sequence was confirmed by Sanger sequencing. Lenti-hSyn-
1260 V5-COX4-APEX2 (hSyn-V5-Mito-APEX2) lentiviruses with the VSV-G pseudo-type were
1261 generated by the St. Jude Viral Vector Core.

1262 Lentiviral vectors prepared at 1-3bn TU/mL were added to organoids in the bioreactor at
1263 200×. For vectors at lower titer, 2 µg/mL Polybrene was also added to the media. After 18–20 h,
1264 organoids were washed twice with DMEM:F12 and fed with fresh media. Media changes were
1265 continued according to the protocol. Lentiviral expression was detected at 72 h posttransduction.
1266

1267 **Immunofluorescence and light microscopy**

1268 Organoids were briefly rinsed in phosphate-buffered saline (PBS) and then fixed in 4%
1269 paraformaldehyde in PBS overnight at 4°C. Following rinses in PBS, organoids were
1270 cryoprotected by incubation overnight in 30% sucrose in PBS. Organoids were then mounted in
1271 Optimal Cutting Temperature (O.C.T.) Compound (Tissue-Tek). Samples were stored at –80°C
1272 until cryosectioning. Cryosectioning was performed on a Leica CM 3050 cryostat set to –20°C.
1273 Serial sections of 20-µm thickness were mounted onto FisherBrand Superfrost Plus microscope
1274 slides and stored at –20°C.

1275 Slides were briefly rehydrated with PBS and then blocked for 1 h at room temperature in
1276 blocking buffer (PBS, 5% normal donkey serum, 0.2% Triton-X100, 0.02% sodium azide, filter
1277 sterilized). Slides were incubated overnight at 4°C in primary antibodies diluted in blocking buffer,
1278 washed with PBS-Tween (0.1%), and incubated 1 h at room temperature in secondary antibodies
1279 diluted 1:500 in blocking buffer. Slides were then washed with PBS-Tween (0.1%), and nuclei
1280 were labeled with DAPI. Excess DAPI was removed by washing with PBS, and slides were dried
1281 and mounted for imaging using Prolong Diamond (Thermo Fisher, P36961). Images were
1282 acquired on a Zeiss Axio Imager M2 equipped with a 20× Plan-Apochromat Objective (Zeiss, 0.8
1283 NA), 40× EC Plan-NeoFluar Objective (Zeiss, 1.3 NA), and Apotome.2 (Zeiss). Images including
1284 GABA were acquired using the 40× objective. All other images were acquired using the 20×

1285 objective. During imaging, exposure times were kept below saturation, and imaging conditions
1286 were constant within experiments. For images acquired with the Apotome.2, Z-series were
1287 acquired at software-recommended intervals and image stacks were then deconvolved using ZEN
1288 software and a constrained iterative algorithm. Images are shown as maximum intensity
1289 projections prepared in Zeiss ZEN 3.7 software.

1290 The following primary antibodies and dilutions were used: TCF7L2 (Cell Signaling
1291 Technologies 2569, 1:1000), OTX2 (R&D Systems AF1979, 1:100), TUBB3 (Abcam Ab107216,
1292 1µg/mL), SOX2 (R&D Systems MAB2018, 1:200), V5 (Invitrogen R960-25, 1:1000), FOXP2
1293 (Abcam ab16046, 1:250), LHX2 (Sigma ABE1402,1:250), GBX2 (R&D Systems AF4638, 1:250),
1294 and GABA (Sigma A2052, 1:5000). The following $f(ab')_2$ secondary antibodies from Jackson
1295 Immunoresearch were used: donkey anti–rabbit Alexa Fluor (AF) 488 (711-546-152), donkey
1296 anti–goat AF 647 (705-606-147), donkey anti–mouse AF 488 (715-546-150), donkey anti–mouse
1297 AF 647 (715-606-150), and donkey anti–chicken AF 647 (703-606-155).

1298

1299 **Bulk RNA-seq**

1300 Each sample consisted of 2-3 pooled organoids from the indicated condition. Total RNA was
1301 isolated using the Direct-zol RNA Microprep Kits (Zymo, R2061), and DNA contamination was
1302 removed using the DNA-free DNA Removal Kit (Thermo Fisher, AM1906). RNA was quantified
1303 using the Quant-iT RiboGreen RNA assay (ThermoFisher) and quality checked by the 2100
1304 Bioanalyzer RNA 6000 Nano assay (Agilent) or 4200 TapeStation High Sensitivity RNA
1305 ScreenTape assay (Agilent) prior to library generation. Libraries were prepared from total RNA
1306 with the TruSeq Stranded mRNA Library Prep Kit, according to the manufacturer's instructions
1307 (Illumina PN 20020595). Libraries were analyzed for insert-size distribution using the 2100
1308 BioAnalyzer High Sensitivity kit (Agilent), 4200 TapeStation D1000 ScreenTape assay (Agilent),
1309 or 5300 Fragment Analyzer NGS fragment kit (Agilent). Libraries were quantified using the Quant-
1310 iT PicoGreen ds DNA assay (ThermoFisher) or by low-pass sequencing with a MiSeq nano kit

1311 (Illumina). Paired-end 100-cycle sequencing was performed on a NovaSeq 6000 (Illumina) in the
1312 St. Jude Hartwell Center Genome Sequencing Core.

1313 For tdTomato-expression analysis, we built a custom reference genome by adding the
1314 tdTomato sequence to the human genome (hg38, gencode v31). The tdTomato sequence was
1315 also added to the gene-annotation gtf file (gencode v31). Read alignment to the custom genome
1316 was performed with STAR (version 2.7) software.[108] Gene-level read count was determined using
1317 RSEM (version 1.3.1).[109]

1318 For differential gene expression analysis, only protein-coding genes validated at
1319 GENECODE confidence level 1 to 3 were considered. To remove genes that were lowly
1320 expressed, we first calculated the cutoff as 10 read counts per million library size, where the library
1321 size was defined as the median library size in the data set. We then kept genes with expression
1322 level (counts per million) equal to or above the cutoff in a minimum number of samples, where
1323 the number of samples was chosen according to the minimum group sample size. The data were
1324 then normalized by TMM function in edgeR package,[110] followed by the limma package with its
1325 voom method, linear modeling, and empirical Bayes moderation to assess differential
1326 expression.[111]

1327 Markers of interest were identified by performing a differential-expression analysis using
1328 *BrainSpan* Developmental Transcriptome data. Thalamic structures (mediodorsal nucleus of the
1329 thalamus and dorsal thalamus) were compared with all cortical structures. The top 100 up- or
1330 down-regulated genes in thalamic vs cortical structures were identified as “thalamic” or “cortical”
1331 markers, respectively.

1332 Deconvolution of bulk RNA-seq data was performed using the VoxHunt (v1.0.1)[112] R
1333 package using the default workflow
1334 (https://quadbio.github.io/VoxHunt/articles/deconvolution.html). *Allen Brain Atlas* data derived
1335 from E13 mouse brain were used as a reference. The “broad” gene set contained the top 50

1336 markers for each region of interest. The top 15 markers were then used as input for the
1337 deconvolution tool.

1338 GO term enrichment analysis was performed using g:Profiler.[113] For all analyses, a custom
1339 background was uploaded containing genes detected in the data set of interest. Driver terms
1340 containing fewer than 300 genes were selected for graphing. All graphs, except heatmaps, were
1341 prepared in R using ggplot2 (v3.4.0).[114] Heatmaps were prepared using the ComplexHeatmap
1342 (v2.10.0) R package.[115,116]

1343

1344 **RT-qPCR**

1345 RNA was isolated and DNase-treated, as described above. Reverse transcription was performed
1346 using 100 ng RNA and the iScript cDNA Synthesis Kit (Bio-Rad, 1708891). A qPCR analysis was
1347 then performed using SYBR Green Master Mix (Thermo Fisher, 4309155) and a C1000 Touch
1348 Thermal Cycler (Bio-Rad). The following primers were used: *GAPDH* Forward 5′-
1349 AATCCCATCACCATCTTCCA-3′, *GAPDH* Reverse 5′-TGGACTCCACGACGTACTCA-3′,
1350 *TCF7L2* Forward 5′-GAATCGTCCCAGAGTGATGTCG-3′, *TCF7L2* Reverse 5′-
1351 TGCACTCAGCTACGACCTTTGC-3′, *OLIG3* Forward 5′-TGAGGCTGAAGATCAACGGACG-3′,
1352 *OLIG3* Reverse 5′-AGTTTCTGGCGAGCAGGAGTGT-3′, *GBX2* Forward 5′-
1353 GCGGAGGACGGCAAAGGCTTC-3′, *GBX2* Reverse 5′-GTCGTCTTCCACCTTTGACTCG-3′,
1354 *LHX9* Forward 5′-ACCTGCTTTGCCAAGGACGGTA-3′, *LHX9* Reverse 5′-
1355 TGACCATCTCCGAGGCGGAAAT-3′, *OTX2* Forward 5′-GGAAGCACTGTTTGCCAAGACC-3′,
1356 *OTX2* Reverse 5′-CTGTTGTTGGCGGCACTTAGCT-3′, *FOXG1* Forward 5′-
1357 GTATGTGGTCACTAACAGGTC-3′, and *FOXG1* Reverse 5′-ACCACAGTATCACAATCAAG-3′.

1358 Data were analyzed using the $2^{-\Delta\Delta Cq}$ method [previously known as the $2^{-\Delta\Delta Ct}$ method, first
1359 described in the Applied Biosystems User Bulletin 2 (P/N 4303859)].[117] Transcripts of interest
1360 were normalized first to *GAPDH* (within sample), then to the mean ΔCq of the hThO samples with
1361 high tdTomato that were previously used for bulk RNA-seq. Regression analyses were performed

1362 in R using normalized values and graphed using the ggscatter function from ggpubr (v0.5.0). For
1363 all transcripts, except *FOXG1*, r and p were calculated using the Pearson correlation method,
1364 where *r* represents the correlation coefficient and p represents the p-value, and lines were fit using
1365 linear regression. Due to the presence of extreme outliers, for *FOXG1* the r_s and p-valuewere
1366 calculated using the Spearman correlation method, in which r_s represents the correlation
1367 coefficient, p represents the p-value, and the nonlinear curve is fit using the Loess local
1368 polynomial-regression method.
1369

1370 **Preparation and sequencing of the snRNA-seq library**

1371 Two independent biological replicates were performed per the differentiation protocol (either
1372 cortical or thalamic), each containing 36 organoids pooled together. The hThOs were D91 or D96;
1373 the hCOs were D91. All organoids were flash frozen in liquid nitrogen and stored at –80°C until
1374 dissociation. Nuclei dissociation was performed as previously described.[118] Briefly, frozen tissue
1375 was mechanically dissociated with a Dounce homogenizer in detergent lysis buffer containing
1376 0.32 M sucrose, 10 mM HEPES (pH 8.0), 5 mM $CaCl_2$, 3 mM magnesium acetate, 0.1 mM EDTA,
1377 1 mM DTT, and 0.1% Triton-X100. The resulting homogenate was filtered through a 40-µm
1378 strainer and washed with the same solution described, without the Triton-X100 added. Nuclei
1379 were then centrifuged at 3200 ×*g* for 10 min at 4°C, and the supernatant was decanted. A sucrose-
1380 dense solution containing 1 M sucrose, 10 mM HEPES (pH 8.0), 3 mM magnesium acetate, and
1381 1 mM DTT was carefully layered underneath the remaining supernatant and then spun at 3200
1382 ×*g* for 20 min at 4°C. The supernatant was discarded, and the final remaining nuclei were
1383 resuspended in 0.4 mg/mL BSA and 0.2 U/µL Lucigen RNAse inhibitor (catalog number 30281-
1384 1) diluted in PBS. Between 5000 and 10,000 nuclei were inspected and counted on a
1385 hemacytometer before loading onto the 10× Chromium Controller (10× Genomics, catalog
1386 number 1000171). The snRNA-seq libraries were prepared using the 10× Genomics Chromium

1387 Next GEM Single Cell Kit, version 3.1 single index gene expression profiling assay, according to
1388 the manufacturer's instructions.

1389 Libraries were analyzed for insert-size distribution by using the 2100 BioAnalyzer High
1390 Sensitivity kit (Agilent), 4200 TapeStation D1000 ScreenTape assay (Agilent), or 5300 Fragment
1391 Analyzer NGS fragment kit (Agilent). Libraries were quantified using the Quant-iT PicoGreen ds
1392 DNA assay (ThermoFisher) or by low-pass sequencing with a MiSeq nano kit (Illumina). Paired-
1393 end 100-cycle sequencing was performed on a NovaSeq 6000 (Illumina) in the St. Jude Hartwell
1394 Center Genome Sequencing Core.

1395

1396 **Analysis of snRNA-seq data**

1397 Sequences from each Illumina-sequencing data set were de-multiplexed using bcl2fastq
1398 v2.20.0.422 (Illumina). The sequencing data were aligned to the human reference genome
1399 GRCh38 (10× Genomics, v2020-A) using the CellRanger "count" algorithm (10× Genomics,
1400 v7.0.0); however, the "–force-cells" option was set to the estimated number of cells loaded for
1401 each sample (snCBO1: 6,000; snCBO2: 8,000; snTha1: 8,000; snTha2: 10,000). From the gene
1402 expression matrix, the downstream analysis was carried out in R (v4.2.1). First, the ambient RNA
1403 signal was removed using the default SoupX (v1.6.2) workflow (autoEstCounts and adjustCounts;
1404 github.com/constantAmateur/SoupX).[119]

1405 Each data set was initially filtered so that genes that were expressed in at least three cells,
1406 and cells that expressed at least 200 genes were included. Additionally, cells with fewer than 300
1407 genes (presumed to be droplets or cellular debris), fewer than 500 UMIs, more than 1% unique
1408 transcripts derived from mitochondrial genes, or more than 3 median absolute deviations (MADs)
1409 from the median number of unique transcripts derived from mitochondrial genes were removed.
1410 Afterwards, cells with more than 3 MADs from the median number of genes expressed were
1411 removed.

1412 Samples were then preprocessed using the standard Seurat (v4.3.0) workflow
1413 (NormalizeData, ScaleData, FindVariables, RunPCA, FindNeighbors, FindClusters, and
1414 RunUMAP; github.com/satijalab/Seurat).[120–123] Data sets were individually log-normalized using
1415 Seurat's NormalizeData with default parameters. Cell cycle scoring was conducted using the
1416 associated S- and G2M-phase gene list from Tirosh et al.[124] and the CellCycleScoring command
1417 in Seurat. We calculated 3000 features exhibiting high cell-to-cell variation in the data set by using
1418 Seurat's FindVariableFeature function. Next, we scaled the data by linear regression against the
1419 number of reads by using Seurat's ScaleData function with default parameters. The variable
1420 genes were projected onto a low-dimensional subspace by performing principal component
1421 analysis using Seurat's RunPCA function with default parameters. The number of principal
1422 components (n = 30) was selected based on inspection of the plot of variance explained.

1423 Data sets were integrated using Harmony (v 0.1.1) with default parameters.[125] A shared-
1424 nearest-neighbor graph was constructed based on the Euclidean distance in the low-dimensional
1425 subspace using Seurat's FindNeighbors with dims = 1:30 and default parameters. Integrated data
1426 sets then underwent nonlinear dimensional reduction and visualization using UMAP. Clusters
1427 were identified using a resolution of 0.4 and the Leiden algorithm for the integrated data sets.
1428 Pseudotime analysis was conducted using Monocle3 (v1.3.1) with default parameters.[126–129]
1429 Trajectory starting points were manually selected based on the expression of mitotic markers
1430 (e.g., *MKI67*) and/or neural precursor markers (e.g., *TNC*). Mapping of snRNA-seq data sets onto
1431 *Allen Brain Atlas* and *BrainSpan* reference data sets was performed using the VoxHunt (1.0.1) R
1432 package with the suggested workflows
1433 (https://quadbio.github.io/VoxHunt/articles/getting_started.html;
1434 https://quadbio.github.io/VoxHunt/articles/other_references.html).[112] For *Allen Brain Atlas*
1435 comparisons, data derived from E15 mouse embryos were used. For *BrainSpan* comparisons,
1436 data derived from human fetal tissue 13–24 postconception weeks (pcw) were used. Neural
1437 communication patterns were predicted and visualized using the NeuronChat (v1.0.0) R package

1438 with the suggested workflow (https://github.com/Wei-
1439 BioMath/NeuronChat/blob/main/vignettes/NeuronChat-Tutorial.html).[62]
1440 Cell types were assigned to each cell/cluster based on marker expression and cell cycle
1441 analysis. For hThO annotation, markers of interest were identified based on a comparison to
1442 previously published scRNA-seq or snRNA-seq studies in developing mouse thalamus or
1443 diencephalon.[130,131] Additional markers were identified based on previously published *in situ*
1444 studies examining embryonic rodent thalamus. For example, within the mouse thalamus[132] and
1445 hThOs, *SOX2* is expressed in a subset of postmitotic neurons. For hCO cluster annotation,
1446 markers of interest were identified using a previously published scRNA-seq study that examined
1447 human neocortex at midgestation.[51] Additional markers were identified based on previously
1448 published *in situ* studies examining embryonic rodent cortex.
1449
1450 **Electron microscopy for DAB-labeled samples**
1451 Prior to fusion, TCF7L2-tdTomato$^+$ thalamic and VGLUT1-tdTomato$^+$ hSyn-GFP$^+$ cortical
1452 organoids were separately transduced in low-attachment 6-well plates with 10^7 TU/mL Lenti-
1453 hSyn-V5-COX4-APEX2 lentiviral vector. After 18–20 h, organoids were washed twice with
1454 DMEM:F12 and fed fresh media. After 3 days, APEX2-transduced thalamic organoids were fused
1455 with cortical organoids, and APEX2-transduced cortical organoids were fused with thalamic
1456 organoids to generate the assembloids described above. At 6–7 weeks postfusion, the
1457 assembloids were prepared for electron microscopy analysis. Specifically, each assembloid was
1458 embedded at the center of a UV-sterilized Nunc Thermanox plastic coverslip (Thermo Fisher,
1459 174950) in 5 µL GFR-Matrigel for 1 h at 37°C. They were then transferred to the fusion media in
1460 6-well plates and placed in the incubator overnight. The following day, a sterile blade was used
1461 to cut a V-shaped notch out of the coverslip on the side containing the APEX2$^+$ half of the
1462 assembloid. DAB labeling was then performed using an adapted protocol.[133]

1463 Briefly, after 1 additional day at 37°C, assembloids were fixed for 1 h in 2% glutaraldehyde
1464 in 0.1 M sodium cacodylate at room temperature, after which the fixative was replaced, and
1465 samples were incubated 1 h at 4°C. The samples were then washed thrice for 5 min in ice-cold
1466 wash solution (0.1 M sodium cacodylate). Next, the samples were incubated 5 min in 20 mM
1467 glycine in 1× sodium cacodylate, then washed thrice for 5 min on ice. The samples were
1468 preincubated in 0.5 mg/mL DAB in 0.1 M sodium cacodylate for 30 min on ice. The samples then
1469 underwent DAB staining in 0.5 mg/mL DAB and 50 mM H_2O_2 in 0.1 M sodium cacodylate on ice.
1470 The reaction was terminated by washing the samples thrice for 5 min on ice in wash solution.
1471 After the DAB labeling developed, samples were postfixed in 2% osmium tetroxide in 0.1
1472 M cacodylate buffer on ice for 30 min. Samples were subsequently washed 5 times for 2 min in
1473 ice-cold water, and then they were contrasted with 2% uranyl acetate overnight at 4°C. Samples
1474 were washed five times for 2 min in ice-cold water. Samples were dehydrated on ice by an
1475 ascending series of ethanol to 100%, followed by 100% propylene oxide at room temperature.
1476 Samples were infiltrated with EmBed-812 and polymerized at 60°C. Embedded samples were
1477 sectioned at ~70 nm on a Leica ultramicrotome and examined in a ThermoFisher Scientific TF20
1478 transmission electron microscope at 80 kV. Digital micrographs were captured with an Advanced
1479 Microscopy Techniques imaging system. Unless otherwise indicated, all reagents were from
1480 Electron Microscopy Sciences.
1481
1482 **Identification of synapses by transmission electron microscopy**
1483 Individual organoids were harvested between D102 and D121 for electron microscopy imaging.
1484 Samples were fixed in 0.1 M cacodylate buffer containing 2.5% glutaraldehyde and 2%
1485 paraformaldehyde. Samples were postfixed in reduced osmium tetroxide and contrasted with
1486 aqueous uranyl acetate. Dehydration was by an ascending series of ethanol to 100%, followed
1487 by 100% propylene oxide. Samples were infiltrated with EmBed-812 and polymerized at 60°C.
1488 Embedded samples were sectioned at ~70 nm on a Leica ultramicrotome and examined in a

1489 ThermoFisher Scientific TF20 transmission electron microscope at 80 kV. Digital micrographs
1490 were captured with an Advanced Microscopy Techniques imaging system. Unless otherwise
1491 indicated, all reagents were from Electron Microscopy Sciences.
1492
1493 **Fusion of 2-dimensional organoids**
1494 TCF7L2-tdTomato$^+$ thalamic and VGLUT1-tdTomato$^+$ hSyn-GFP$^+$ cortical organoids were halved
1495 using a pair of ultra-fine clipper scissors and plated in a culture-insert 2-well in μ-dish 35 mm
1496 (81176, Ibidi). Specifically, each half chamber was first coated with human ES-qualified Matrigel
1497 diluted 1:200 in DMEM:F12, for 1 h at room temperature. The coating solution was aspirated and
1498 100 μL fusion media was added to each half. One thalamic organoid half was placed in one
1499 chamber and 1-2 cortical organoid halves were placed in the other and allowed to attach and
1500 extend neural processes for 5 days. On D5, the barrier was removed using sterilized blunt forceps,
1501 and the organoids were maintained in culture with media changes every 7 days. The barrier region
1502 in each dish was imaged every 3–7 days, from D9 to D61, at the same exposure time on a Zeiss
1503 AxioObserver D1.
1504
1505 **Whole-cell patch-clamp electrophysiology**
1506 Whole-cell recordings were made in individual organoids between D90 and D141 or in
1507 assembloids between D19 and D78 postfusion. Organoids were placed in a recording chamber
1508 mounted on a two-photon laser-scanning microscope (Bruker) and superfused (2-3 mL/min) with
1509 aCSF containing the following solution: 125 mM NaCl, 2.5 KCl, 2 mM $CaCl_2$, 2 mM $MgCl_2$, 1.25
1510 mM NaH_2PO_4, 26 mM $NaHCO_3$, and 20 mM glucose at 300–310 mOsm, equilibrated with 95%
1511 O_2/5% CO_2 at 32°C.
1512 Cells were visualized under two-photon guidance by using PrairieView v5.5 software.
1513 Whole-cell voltage- and current-clamp recordings were made from visually identified thalamic or
1514 cortical cells. Short-term synaptic plasticity, 1-Hz induction of LTD, and 40-Hz LTP were recorded

1515 in voltage-clamp mode (V_{Hold} = –60 mV), with an internal pipette containing the following solution:
1516 125 mM $CsMeSO_3$, 2 mM CsCl, 10 mM HEPES, 0.1 mM EGTA, 4 mM ATP-Mg_2, 0.3 mM GTP-
1517 Na, 10 mM creatine phosphate-Na_2, 5 mM QX-314 chloride, and 5 mM TEA-Cl at pH 7.4 and 290-
1518 295 mOsm. Borosilicate glass pipettes (Sutter, 3-6 MΩ open pipette resistance) were used.

1519 For investigating membrane properties and LTP induced by the STDP protocol, the
1520 internal solution contained 115 mM potassium gluconate (KGlu), 20 mM KCl, 10 mM HEPES, 4
1521 mM $MgCl_2$, 0.1 mM EGTA, 4 mM ATP-Mg_2, 0.4 mM GTP-Na, and 10 mM creatine phosphate-Na_2
1522 at pH 7.4 and 290-295 mOsm. Recordings were obtained using a Multiclamp 700B amplifier (Axon
1523 Instruments). Signals were digitized with an Axon Digidata 1550B (Axon Instruments) at 20 kHz
1524 and filtered at 2 kHz using Clampex 10.7 software. The liquid-junction potential was calculated to
1525 be –10 mV and was corrected for in each recording.

1526 In current-clamp experiments, the rheobase was measured by first injecting a
1527 hyperpolarizing current step (–20 pA), followed by a depolarizing ramp (from –20 pA to +200 pA)
1528 into cells. The current at which the first AP was generated was recorded and averaged across
1529 cells. A series of hyperpolarizing and depolarizing step currents were injected into cells in current-
1530 clamp mode (+10 pA steps from –50 pA to +240 pA for 1 s) to measure input resistance and
1531 evoked firing rates.

1532 In voltage-clamp experiments, synaptic currents were evoked using a bipolar concentric
1533 stimulating electrode (World Precision Instruments) or a homemade 2-prong stimulating electrode
1534 connected to a stimulus-isolation unit (Iso-Flex, A.M.P.I.) positioned in either the thalamic or
1535 cortical side of assembloids. Stimulus intensities were adjusted prior to each experiment to elicit
1536 measurable EPSCs in cortical or thalamic neurons. Because of the variability between
1537 assembloids, the amplitudes of evoked EPSCs ranged from –20 pA to –300 pA. PPRs were
1538 measured by delivering 2 stimuli 50, 100, 200, 500, or 1000 ms apart for both TC and CT
1539 synapses.

1540 TC LTP was induced by high-frequency stimulation: 10 trains of 40-Hz stimulation for 200
1541 ms every 5 s, repeated 3× every 5 min.[80] Additional TC LTP and CT LTP were induced via an
1542 STDP protocol: a single presynaptic electrical stimulation preceded four postsynaptic APs by 10
1543 s. Postsynaptic APs were induced by four somatic current injections of 2 nA (2-ms duration) at 40
1544 Hz. This protocol was repeated 50 times (at 1 Hz) every 5 min, for a total of three times (long
1545 STDP-induction protocol).[134] In a subset of experiments, the STDP protocol was delivered only 1×
1546 (short STDP-induction protocol). LTD was induced at TC and CT synapses by delivering electrical
1547 low-frequency stimulation at 1 Hz for 900 pulses.[135] In all long-term synaptic plasticity induction
1548 protocols, cells were current-clamped at –60 mV. EPSC peak amplitudes were measured before
1549 and after synaptic plasticity induction in voltage-clamp mode (V_{hold} = –60 mV) using paired
1550 electrical stimulation (10 Hz) delivered every 20 s for a 5-min baseline period and a 30-min
1551 postinduction period.

1552 All electrophysiological experiments were analyzed offline using Clampfit 10.7 software.
1553 For all long-term synaptic plasticity experiments, raw EPSC amplitudes were measured, averaged
1554 per minute, and expressed as a percent change from baseline. The amplitude of the first EPSC
1555 peak was measured if a polysynaptic response was elicited. To determine a change in synaptic
1556 strength after the plasticity-induction protocols, the full postinduction time periods of all the cells
1557 in the experiment were averaged and compared to a theoretical baseline of 100% by using a one-
1558 sample *t*-test (GraphPad Prism 8.4.2), unless noted. To compare between experimental drug
1559 conditions, a one-way ANOVA with Dunnett's multiple comparisons post-hoc test was used. PPR
1560 was calculated by measuring the peak amplitude of the evoked EPSC from both pulses and
1561 dividing the EPSC2 peak amplitude by the EPSC1 peak amplitude. The PPR for each ISI of each
1562 synapse was compared against 1.0 by using a one-sample *t*-test and between TC and CT
1563 synapses by using an unpaired two-tailed *t*-test.
1564

1565 **Two-photon calcium imaging**

1566 Two-photon calcium imaging was performed as described previously.[63] Briefly, two-photon laser-
1567 scanning microscopy was performed using an Ultima imaging system (Bruker), a Ti:sapphire
1568 Chameleon Ultra femtosecond-pulsed laser (Coherent, 820 nm) and 60× [0.9 numerical aperture]
1569 water-immersion infrared objectives (Olympus). Fluo-5F (300 μM) and Alexa 594 (10-25 μM) were
1570 included in the internal solution containing 115 mM potassium gluconate, 20 mM KCl, 10 mM
1571 HEPES, 4 mM $MgCl_2$, 0.1 mM EGTA, 4 mM ATP-Mg_2, 0.4 mM GTP-Na, 5 mM QX-314 chloride,
1572 and 10 mM creatine phosphate-Na_2 at pH 7.4 and 290-295 mOsm. Synaptically evoked changes
1573 in fluorescence of both fluorophores were measured in line-scan mode in a dendritic spine and
1574 the parent dendritic shaft. Line scans were analyzed as a ratio of normalized green (G) (Fluo-5F)
1575 fluorescence to normalized red (R) (Alexa Fluor 594) fluorescence (G/R). A line-scan was
1576 performed through every visible dendritic spine on a targeted dendritic branch, in an orientation
1577 that was parallel to the dendritic spine neck and orthogonal to the dendritic shaft.

1578

1579 **Statistical analyses**

1580 Statistical tests were performed using Prism (Graphpad) or Sigmaplot (Systat) software.
1581 Statistical comparisons are noted in the text or figure legends. Unless otherwise noted,
1582 distributions were tested for normality (Shapiro-Wilk test) and equal variance (Brown-Forsythe
1583 test). If the distribution passed, a paired or unpaired *t*-test was performed. If it failed, a rank-sum
1584 test or signed-rank test was performed. To compare more than two distributions, a one-way or
1585 repeated-measures ANOVAs was performed. Significance was designated as $P < 0.05$. All data
1586 are presented as the mean ± SEM, and the sample size (N) is presented as the number of cells
1587 per the number of assembloids.

1588

1589 **Drugs**

1590 All salts for aCSF were purchased from Sigma-Aldrich. QX-314 chloride was purchased from
1591 Hello Bio. DL-AP5 and MPEP were purchased from Tocris Bioscience. To create stock
1592 solutions, MPEP was dissolved in DMSO and DL-AP5 was dissolved in water; both were kept
1593 frozen at –20°C until dilution in aCSF to the final concentration. For iBAPTA experiments,
1594 BAPTA tetra-potassium salt and BAPTA tetra-cesium salt were included in KGlu- and Cs-based
1595 intracellular solutions, respectively, at 20 mM.

1596

1597